Lawrence Berkeley National Laboratory

Title

SARS-CoV-2 RBD antibodies that maximize breadth and resistance to escape

Permalink

https://escholarship.org/uc/item/88q0b6b7

Journal

Nature, 597(7874)

ISSN

0028-0836

Authors

Starr, Tyler N
Czudnochowski, Nadine
Liu, Zhuoming
et al.

Publication Date

2021-09-02

DOI

10.1038/s41586-021-03807-6

Peer reviewed

SARS-CoV-2 RBD antibodies that maximize breadth and resistance to escape

Tyler N. Starr[1,*], Nadine Czudnochowski[2,*], Zhuoming Liu[3,*], Fabrizia Zatta[4], Young-Jun Park[5], Amin Addetia[1], Dora Pinto[4], Martina Beltramello[4], Patrick Hernandez[2], Allison J. Greaney[1,6], Roberta Marzi[4], William G. Glass[7], Ivy Zhang[7,8], Adam S. Dingens[1], John E. Bowen[5], M. Alejandra Tortorici[5], Alexandra C. Walls[5], Jason A. Wojcechowskyj[2], Anna De Marco[4], Laura E. Rosen[2], Jiayi Zhou[2], Martin Montiel-Ruiz[2], Hannah Kaiser[2], Josh Dillen[2], Heather Tucker[2], Jessica Bassi[4], Chiara Silacci-Fregni[4], Michael P. Housley[2], Julia di Iulio[2], Gloria Lombardo[4], Maria Agostini[2], Nicole Sprugasci[4], Katja Culap[4], Stefano Jaconi[4], Marcel Meury[2], Exequiel Dellota[2], Rana Abdelnabi[9], Shi-Yan Caroline Foo[9], Elisabetta Cameroni[4], Spencer Stumpf[3], Tristan I. Croll[10], Jay C. Nix[11], Colin Havenar-Daughton[2], Luca Piccoli[4], Fabio Benigni[4], Johan Neyts[9], Amalio Telenti[2], Florian A. Lempp[2], Matteo S. Pizzuto[4], John D. Chodera[7], Christy M. Hebner[2], Herbert W. Virgin[2,12,13], Sean P.J. Whelan[3], David Veesler[5], Davide Corti[4,†], Jesse D. Bloom[1,6,14,†], Gyorgy Snell[2,†]

[1]Basic Sciences Division, Fred Hutchinson Cancer Research Center, Seattle, WA 98109, USA
[2]Vir Biotechnology, San Francisco, CA 94158, USA
[3]Department of Molecular Microbiology, Washington University School of Medicine, St. Louis, MO 63110, USA
[4]Humabs BioMed SA, a subsidiary of Vir Biotechnology, 6500 Bellinzona, Switzerland
[5]Department of Biochemistry, University of Washington, Seattle, WA 98195, USA
[6]Department of Genome Sciences, University of Washington, Seattle, WA 98195, USA
[7]Computational and Systems Biology Program, Sloan Kettering Institute, Memorial Sloan Kettering Cancer Center, New York, NY 10065, USA
[8]Tri-Institutional PhD Program in Computational Biology and Medicine, Weill Cornell Graduate School of Medical Sciences, New York, NY 10065, USA
[9]Rega Institute for Medical Research, Laboratory of Virology and Chemotherapy, KU Leuven, Belgium
[10]Cambridge Institute for Medical Research, Department of Haematology, University of Cambridge, Cambridge, CB2 0XY, UK
[11]Molecular Biology Consortium, Advanced Light Source, Lawrence Berkeley National Laboratory, Berkeley, CA 94720, USA
[12]Department of Pathology and Immunology, Washington University School of Medicine, Saint Louis, MO 63110, USA
[13]Department of Internal Medicine, UT Southwestern Medical Center, Dallas, TX 75390, USA
[14]Howard Hughes Medical Institute, Seattle, WA 98109, USA

[*] These authors contributed equally
† Correspondence: dcorti@vir.bio, jbloom@fredhutch.org, gsnell@vir.bio

39   An ideal anti-SARS-CoV-2 antibody would resist viral escape[1–3], have activity against diverse SARS-related

40   coronaviruses (sarbecoviruses)[4–7], and be highly protective through viral neutralization[8–11] and effector

41   functions[12,13]. Understanding how these properties relate to each other and vary across epitopes would aid

42   development of antibody therapeutics and guide vaccine design. Here, we comprehensively characterize

43   escape, breadth, and potency across a panel of SARS-CoV-2 antibodies targeting the receptor-binding

44   domain (RBD). Despite a tradeoff between *in vitro* neutralization potency and breadth of sarbecovirus

45   binding, we identify neutralizing antibodies with exceptional sarbecovirus breadth and a corresponding

46   resistance to SARS-CoV-2 escape. One of these antibodies, S2H97, binds with high affinity across all

47   sarbecovirus clades to a previously undescribed cryptic epitope and prophylactically protects hamsters

48   from viral challenge. Antibodies targeting the ACE2 receptor binding motif (RBM) typically have poor

49   breadth and are readily escaped by mutations despite high neutralization potency. Nevertheless, we

50   characterize one potent RBM antibody (S2E12[8]) with breadth across sarbecoviruses related to SARS-CoV-

51   2 and a high barrier to viral escape. These data highlight principles underlying variation in escape,

52   breadth, and potency among antibodies targeting the RBD, and identify epitopes and features to prioritize

53   for therapeutic development against the current and potential future pandemics.

54 The most potently neutralizing antibodies to SARS-CoV-2—including those in clinical use[14] and
55 dominant in polyclonal sera[15,16]—target the spike receptor-binding domain (RBD). Mutations in the
56 RBD that reduce binding by antibodies have emerged among SARS-CoV-2 variants[17–21], highlighting the
57 need for antibodies and vaccines that are robust to viral escape. We have previously described an
58 antibody, S309[4], that exhibits potent effector functions and neutralizes all current SARS-CoV-2
59 variants[22,23] and the divergent sarbecovirus SARS-CoV-1. S309 forms the basis for an antibody therapy
60 (VIR-7831, recently renamed sotrovimab) that has received Emergency Use Authorization for treatment
61 of COVID-19[24]. Longer term, antibodies with broad activity across SARS-related coronaviruses
62 (sarbecoviruses) would be useful to combat potential future spillovers[6]. These efforts would be aided by
63 a systematic understanding of the relationships among antibody epitope, resistance to viral escape, and
64 breadth of sarbecovirus cross-reactivity. Here we address this question by comprehensively
65 characterizing a diverse panel of antibodies, including S309, using deep mutational scanning, pan-
66 sarbecovirus binding assays, *in vitro* selection of viral escape, and biochemical and structural analyses.
67
68 *Potency, escapability, and breadth in a panel of RBD antibodies*
69 We identified a panel of anti-SARS-CoV-2 antibodies with distinct properties (**Fig. 1a**, **Extended Data**
70 **Table 1**), including six antibodies newly described in this study. These antibodies bind different epitopes
71 within the receptor-binding motif (RBM) and the non-RBM "core" of the RBD. The antibody panel
72 spans a range of neutralization potencies and binding affinities (**Fig. 1a, Extended Data Fig. 1a-c**).
73
74 We used deep mutational scanning to map how all amino-acid mutations in the SARS-CoV-2 RBD
75 affect binding by each antibody[3] (**Fig. 1b,c** and **Extended Data Fig. 2**). Some antibodies have narrowly
76 focused functional epitopes (the set of residues where mutations abolish binding[25]), with binding-escape
77 mutations at just a few key residues (e.g., S309, S2D106), while other antibodies have wider functional
78 epitopes (e.g., S2H13; tabulations at right in **Fig. 1b,c**). We previously measured how all RBD
79 mutations affect folded RBD expression and ACE2 binding affinity[26] (letter colors in **Fig. 1b,c**). We
80 used the combined measures of how mutations affect antibody binding and RBD function to compute
81 the "escapability" of each antibody, which reflects the extent to which mutations that escape antibody
82 binding are functionally tolerated (**Fig. 1b,c** and **Extended Data Fig. 3a,b**). We also investigated the
83 sensitivity of each antibody to mutations among SARS-CoV-2 sequences reported in GISAID (heatmap
84 below logoplots in **Fig. 1b,c**; **Extended Data Fig. 3c**), and found that some antibodies are more affected
85 by natural SARS-CoV-2 mutations than others, including mutations found in SARS-CoV-2 variants of
86 concern (**Extended Data Fig. 1d**)[27–29].
87
88 We next extended our deep mutational scanning platform to measure binding of each antibody to a pan-
89 sarbecovirus panel of 45 RBDs (**Fig. 1d** and **Extended Data Fig. 4a-f**). The four antibodies that bind
90 the core RBD exhibit cross-reactive binding to RBDs from SARS-CoV-1 and related ACE2-utilizing bat
91 sarbecoviruses, and from sarbecoviruses in Europe and Africa. Antibodies S304 and S2H97 also bind
92 RBDs of the most divergent clade from Asia that have an average 64% amino acid identity with SARS-
93 CoV-2. S2H97 exhibits notably tight binding to all RBDs tested (**Fig. 1d** and **Extended Data Fig. 4f**),
94 making it the broadest pan-sarbecovirus RBD antibody described to date. Antibodies that bind epitopes

95 within the RBM exhibit more limited cross-reactivity, typically binding only SARS-CoV-2 and the
96 closely related GD-Pangolin-CoV RBD. S2E12 stands out among the RBM antibodies we evaluated as
97 it also binds the RaTG13 and GX-Pangolin-CoV RBDs, showing that even within the evolutionarily
98 plastic RBM[19,26] there are epitopes that enable greater breadth than others.
99
100 *The pan-sarbecovirus S2H97 antibody*
101 To understand the structural basis for cross-reactive sarbecovirus binding, we determined the structures
102 of S2H97 Fab (X-ray crystallography, 2.65 Å resolution), S2X35 Fab (X-ray crystallography, 1.83 Å
103 resolution), and S2E12 Fab (X-ray crystallography, 2.95 Å resolution) bound to SARS-CoV-2 RBD
104 (**Fig. 2a** and **Extended Data Table 2**). This panel of cross-reactive antibodies emphasizes the core RBD
105 as a general target of broad antibody binding due to its conservation among sarbecoviruses, reflected in
106 the diverse core RBD surfaces targeted by the broadest of these antibodies (**Fig. 2a** and **Extended Data
107 Fig. 5a-f**).
108
109 The exceptionally cross-reactive S2H97 antibody targets a previously undescribed cryptic antigenic site,
110 which we designated site V (**Fig. 2a,b**). S2H97 binding is facilitated by packing of the heavy chain
111 CDR3 into an RBD crevice at the center of the epitope, together with polar contacts with all three heavy
112 chain CDRs and the light chain CDR2 (**Extended Data Fig. 5f**). Molecular dynamics simulation of the
113 S2H97 Fab:RBD complex highlights the durability of many of these interactions (**Fig. 2b**). The surface
114 bound by S2H97 is constrained by the deleterious effects of mutations on folded RBD expression (**Fig.
115 2b**)[26], and this constraint is likely enhanced by quaternary packing with the NTD in the closed spike
116 trimer (**Extended Data Fig. 6a**). Consistent with the conservation of the S2H97 epitope, S2H97
117 neutralizes diverse sarbecoviruses (**Fig. 2c** and **Extended Data Fig. 4g**) and SARS-CoV-2 variants (**Fig.
118 2d**).
119
120 To understand the evolution of S2H97 breadth, we measured breadth of binding by its germline form,
121 S2H97$_{GL}$, in which we reverted the 13 somatic mutations (**Extended Data Fig. 4h,i**). S2H97$_{GL}$ bound all
122 tested sarbecovirus RBDs and exhibited particularly high affinity for SARS-CoV-2-related RBDs.
123 Somatic mutations enhanced affinity across all sarbecoviruses by two orders of magnitude. This general
124 increase in affinity together with the absence of non-conservative amino acid replacements among
125 paratope residues suggests that framework mutations may contribute to a general improvement in
126 S2H97 binding affinity.
127
128 To characterize the mechanism of S2H97 neutralization, we determined a cryoEM structure of S2H97
129 bound to SARS-CoV-2 S (**Extended Data Fig. 5i-l** and **Extended Data Table 3**). S2H97 binding
130 requires extensive opening of the RBD to unmask its cognate epitope (**Extended Data Fig. 6b**), even
131 more than is required to access the cryptic antigenic site II[15]. Like other antibodies that only bind the
132 open RBD[30,31], S2H97 induces rapid and premature refolding of spike into the post-fusion state (**Fig. 2e**),
133 promotes S1 shedding of cell-surface-expressed spike (**Extended Data Fig. 6c**), and induces a low level
134 of syncytia formation among spike-expressing cells (**Extended Data Fig. 6d**). S2H97 does not interfere
135 with ACE2 binding (**Extended Data Fig. 6e**). Like other non-ACE2-competitive antibodies[31,32], S2H97

136 neutralization is attenuated in cells that over-express ACE2 (**Extended Data Fig. 6f**). Consistent with its
137 ability to neutralize spike-mediated viral entry, S2H97 inhibits spike-mediated cell-cell fusion
138 (**Extended Data Fig. 6g**). Taken together, these experiments suggest that the S2H97 mechanism of
139 neutralization involves receptor-independent conversion of S to the post-fusion state[30], thereby inhibiting
140 ACE2-mediated cell entry.
141
142 Next, we determined the prophylactic efficacy of S2H97 *in vivo* using a Syrian hamster model of
143 infection. We administered hamsters with S2H97 at 25 mg/kg two days prior to intranasal challenge
144 with SARS-CoV-2 and assessed viral RNA load and infectious viral titers in the lungs four days post-
145 infection. S2H97 prophylaxis reduced RNA copies by >10,000-fold relative to control in the four
146 animals that had detectable circulating antibody levels at the time of challenge and reduced infectious
147 viral titers to the lower detection limit in these animals (**Fig. 2f**). The two animals without a reduction in
148 viral load had circulating S2H97 levels below the limit of quantification (50 ng/ml) at the time of viral
149 challenge (**Extended Data Fig. 6h**), which may reflect a failure in the intraperitoneal administration
150 procedure. Therefore, S2H97 demonstrates that antibodies to the newly identified antigenic site V can be
151 protective *in vivo*.
152
153 Last, we performed serum blockade of binding experiments[15], demonstrating that antibodies competing
154 with S2H97 binding are rare in infection- and vaccine-elicited sera (**Fig. 2g**). This sub-dominance of
155 antigenic site V may be explained by the inaccessibility of the epitope as illustrated in the cryoEM
156 structure. However, the protective nature and exceptional breadth of S2H97 suggests that updated
157 immunogen designs, such as those based on the RBD[33–35], could unmask antigenic site V to better elicit
158 S2H97-like antibodies.
159

Variation in breadth and escapability among RBM epitopes

161 Our survey reveals variation in the escapability and breadth of antibodies that target the RBM (**Fig.
162 1c,d**)**,** which is immunodominant (**Fig. 2g**) but variable over sarbecovirus and SARS-CoV-2 evolution.
163 We performed *in vitro* selection experiments to identify spike-expressing VSV mutants that emerge in
164 the presence of each of seven monoclonal antibodies (**Fig. 3a** and **Extended Data Fig. 7a,b**) to further
165 understand escape from these antibodies.
166
167 Many RBM antibodies such as S2X58 and S2D106 select mutations present in SARS-CoV-2 variants of
168 concern (e.g., L452R and E484K)[27–29]. In contrast, S2E12 selects viral mutants at sites that do not exhibit
169 substantial variation among circulating SARS-CoV-2, and S2E12 correspondingly neutralizes a diverse
170 panel of SARS-CoV-2 variants (**Fig. 3b**)[17]. S2E12 is also unique in its breadth among RBM antibodies
171 (**Fig. 1d**), neutralizing VSV pseudotyped with each of the four SARS-CoV-2 clade sarbecovirus spikes
172 (**Fig. 3c** and **Extended Data Fig. 4j**). As with S2H97, somatic mutations in S2E12 enhanced affinity
173 across sarbecoviruses, though the increase in affinity was more modest than for S2H97 (**Extended Data
174 Fig. 4k,l**).
175

176 Conservation of the S2E12 epitope among SARS-CoV-2 variants could reflect the relative rarity of
177 S2E12-like antibodies in polyclonal sera leading to little antigenic pressure at these sites (**Fig. 2g**),
178 together with functional constraint in the S2E12 epitope (escapability being the lowest for S2E12 and
179 S2H97 among the 12 antibodies evaluated). Indeed, the strong antibody-escape mutations that emerged
180 in S2E12 viral escape selections decrease ACE2 binding affinity (**Fig. 3a**)[26] and reduce replicative fitness
181 in a bulk competition experiment between spike-expressing VSV variants passaged in the absence of
182 antibody (**Fig. 3d**).
183
184 To understand the structural basis for the unique breadth and robustness of S2E12 to escape, we
185 compared its structure to that of S2D106 Fab (cryoEM, 4.0 Å resolution local refinement) bound to
186 SARS-CoV-2 RBD (**Fig. 3e,f, Extended Data Fig. 5g,h,m-p and Extended Data Tables 2, 3**). We
187 also integrated evolutionary, functional, and structural details for the sites in each antibody's structural
188 footprint (**Fig. 3g,h**). S2E12 and S2D106 bind the receptor-binding ridge, with 8 residues shared
189 between their footprints. S2E12 binding is oriented toward extensive packing of the ACE2-contact
190 residue $F486_{RBD}$ within a cavity lined by aromatic residues at the antibody light/heavy-chain interface
191 (**Fig. 3e** and **Extended Data Fig. 5g**)**,** as was seen with the homologous antibody COV2-2196[36]. Sites
192 within the S2E12 footprint that exhibit less functional constraint (e.g., E484, S477) are located at the
193 periphery of the interface, explaining the robustness of S2E12 toward SARS-CoV-2 variants (**Fig. 3b,g**).
194 This structural interface also explains the breadth of S2E12 toward RaTG13 and GX-Pangolin-CoV
195 (**Fig. 1d**), as the F486L mutation present in these sarbecoviruses retains the central hydrophobic
196 packing.
197
198 In contrast to S2E12, S2D106 binding is centered on residue $E484_{RBD}$ which may form a salt bridge with
199 $R96_{LC}$, in addition to nonpolar contacts between $F490_{RBD}$ and residues in the heavy chain CDR2 (**Fig. 3f**
200 and **Extended Data Fig. 5h**). Although the long heavy chain CDR3 packs intimately across the surface
201 of the RBD, there are no crucial CDRH3:RBD contacts that are sensitive to mutation. S2D106 escape is
202 therefore highly focused on E484 and F490, which are functionally tolerant and exhibit variation among
203 SARS-CoV-2 sequences (**Fig. 3h**). This comparison between S2E12 and S2D106 highlights how small
204 differences in the RBD:antibody interface impact the breadth and robustness of each antibody to viral
205 escape.
206
207 ***The landscape of RBD epitopes***
208 Last, we examined how escapability, breadth, and neutralization potency relate to one another and to
209 RBD epitope. We used our binding-escape maps (**Fig. 1b,c**), together with comparable maps published
210 for other RBD antibodies[3,20,21,36,37], to project antibodies into a two-dimensional space based on
211 similarities in sites of binding-escape mutations (**Fig. 4a**).
212
213 We annotated our projection of epitope space by antibody properties such as *in vitro* neutralization
214 potency, breadth, and escapability (**Fig. 4b-d** and **Extended Data Fig. 7c,d**). The most potently
215 neutralizing antibodies (e.g., S2E12, S2D106) bind epitopes in the RBM, while antibodies targeting the
216 core RBD are less potently neutralizing (**Fig. 4b**). It is important to note that RBD antibodies can protect

217 *in vivo* through other mechanisms beyond neutralization[12,13,22]. Antibodies with broad sarbecovirus
218 binding target the core RBD (**Fig. 4c**). Our panel therefore extends prior observations[4,5,32,38] to highlight a
219 general tradeoff between sarbecovirus breadth and potency of SARS-CoV-2 neutralization (**Fig. 4e**).
220 Nonetheless, some cross-reactive antibodies exhibit intermediate *in vitro* neutralization potency (e.g.,
221 S309, S2X259[37]), and the highly potent RBM-directed antibody S2E12 exhibits modest breadth,
222 highlighting the existence of antibodies that balance neutralization potency and breadth.
223
224 The size of an antibody's functional epitope (**Fig. 1b,c**) is not strongly influenced by the epitope's
225 structural location (**Extended Data Fig. 7c**)—instead, narrower functional epitopes are associated with
226 higher Fab:RBD binding affinity (**Fig. 4f**). However, an antibody's escapability, which integrates how
227 escape mutations affect RBD folding and ACE2 affinity, is influenced by variation in these functional
228 constraints across the RBD structure. For example, antibodies that cluster with S2E12 exhibit lower
229 escapability (**Extended Data Fig. 7c**) and frequency of natural SARS-CoV-2 escape mutants (**Fig. 4d**).
230 As highlighted in our detailed descriptions of S2E12 and S2H97 above, a modest degree of breadth of
231 sarbecovirus binding is associated with a greatly reduced frequency of escape mutations among
232 circulating SARS-CoV-2 variants (**Fig. 4g**).
233

234 *Principles for optimizing antibody and vaccine development*
235 Ongoing SARS-CoV-2 evolution[19,27–29], long-term antigenic evolution of other human coronaviruses[39,40],
236 and the spillover potential of diverse sarbecovirus lineages[6,7] indicate the importance of developing
237 antibodies and vaccines that are robust to viral evolution. In this work, we identify antibody and epitope
238 features which can guide this process. Although *in vitro* neutralization potency is often prioritized for
239 lead selection, our results suggest this will bias antibodies toward RBM epitopes, many of which are
240 poorly conserved in the short-term evolution of SARS-CoV-2[19] and the long-term evolution of
241 sarbecoviruses[7]. Our results suggest that additional prioritization of high affinity binding and at least a
242 moderate degree of sarbecovirus breadth will yield antibodies with improved resistance to viral escape[4,5].
243

244 A long-term goal is to develop antibodies and vaccines that cross-react with distant sarbecovirus
245 lineages capable of zoonotic spillover. We have identified a cryptic epitope capable of eliciting pan-
246 sarbecovirus immunity, represented by S2H97. Though S2H97-like antibodies are rare in polyclonal
247 sera, the protective capacity and exceptional breadth of S2H97 indicates that pan-sarbecovirus vaccines
248 could seek to improve responses to this epitope by unmasking this and other cryptic broadly neutralizing
249 epitopes[5,37,41]. Broader cross-reactivity among betacoronavirus lineages including MERS and OC43 has
250 been reported for antibodies that bind the spike S2 domain[32,38,42]. Though S2H97 breadth does not extend
251 beyond sarbecoviruses, its discovery expands our view of what can be achieved via a potent RBD-
252 directed antibody response.
253

254 The global emergence of variants of concern (VOCs) has been an important feature of the pandemic[27–29].
255 Mutations in VOCs occur in immunodominant RBM epitopes (e.g., residues E484, K417 and L452) and
256 impact binding by polyclonal serum and some therapeutic antibodies[17–21]. We cannot predict exactly
257 which mutations will next rise to prominence as SARS-CoV-2 continues to evolve, but it seems likely

258   that they will include additional RBM mutations that impact recognition by infection- and vaccine-
259   elicited antibodies[1,2,15,16,19]. Therefore, antibody discovery efforts focused on breadth[4,5], aided by high-
260   resolution differentiation among antibody epitopes as generated herein, can inform the development of
261   antibody and vaccine countermeasures with greater robustness to immune escape in the current SARS-
262   CoV-2 pandemic and utility for potential future sarbecovirus spillovers.
263

AUTHOR CONTRIBUTIONS

Conceived research and designed study: TNS, NC, HWV, DC, JDB, GS. Antibody discovery: FZ, DP, MB, RM, ADM, EC, MSP, DC. Expression and purification of proteins: NC, PH, GL, NS, JEB, ACW, KC, SJ, MM. Antibody functional experiments: YJP, ZL, FZ, DP, MB, RM, JEB, MAT, ACW, JAW, ADM, LER, JZ, MMR, HK, JD, HT, JB, CSF, MPH, MA, ED, SS, CHD, LP, FB, FAL, SPJW. Deep mutational scanning experiments and analysis: TNS, AA, AJG, ASD. Hamster model: RA, SCF, FB, JN. Bioinformatics analysis: JDI, AT. Structure determination: NC, YJP, PH, JEB, TIC, JCN, DV, GS. Molecular dynamics simulation and analysis: WGG, IZ, JDC. Supervision: MSP, JDC, CMH, SPJW, DV, DC, JDB, GS. Wrote the initial draft: TNS, NC, DC, JDB, GS. Edited the final version: all authors.

DECLARATION OF INTERESTS

Additional Information

Correspondence and requests for materials should be addressed to Davide Corti (dcorti@vir.bio), Jesse D. Bloom (jbloom@fredhutch.org), and Gyorgy Snell (gsnell@vir.bio).

MATERIALS AND METHODS

Mammalian cell lines

Cell lines were received from ATCC (Vero E6, Vero, BHK-21, CHO-K1, HEK293T/17), Takara (Lenti-X 293T) and Thermo Fisher Scientific (ExpiCHO-S, Expi293F and Freestyle 293-F). MA104 cells were a gift from Harry Greenberg. 293T-ACE2 cells are described in references [31] and [43]. Vero and MA104 cell lines tested negative for mycoplasma contamination. Other cell lines were not tested. No authentication was performed beyond manufacturer standards.

Isolation of peripheral blood mononuclear cells (PBMCs), plasma and sera

Samples from three SARS-CoV-2 recovered individuals, designated as donors S2H (age 36, male), S2D (age 70, male) and S2X (age 52, male) were obtained under study protocols approved by the local Institutional Review Board (Canton Ticino Ethics Committee, Switzerland). All donors provided written informed consent for the use of blood and blood components (such as PBMCs, sera or plasma). Blood drawn from donor S2X was obtained at day 48 (S2X16, S2X35 and S2X58 antibodies) and 75 (S2X227) after symptoms onset. Blood from donor S2H was obtained at day 17 (S2H13 and S2H14), day 45 (S2H58) and day 81 (S2H97) after symptoms onset. Blood from donor S2D was obtained at day 98 (S2D106) after symptoms onset.

PBMCs were isolated from blood draw performed using tubes pre-filled with heparin, followed by Ficoll density gradient centrifugation. PBMCs were either used fresh for SARS-CoV-2 Spike protein-specific memory B cell sorting or stored in liquid nitrogen for later use. Sera were obtained from blood collected using tubes containing clot activator, followed by centrifugation and storage at -80°C.

Sera for blockade of binding serological assays were obtained from 3 cohorts of SARS-CoV-2 convalescent (average age 52, range 25–78, 55% male) or vaccinated (average age 49, range 28–69, 65% male) individuals under study protocols approved by the local Institutional Review Boards (Canton Ticino Ethics Committee, Switzerland, the Ethical Committee of Luigi Sacco Hospital, Milan, Italy, and WCG North America, Princeton, NJ, USA). All donors provided written informed consent for the use of blood and blood components (such as PBMCs, sera or plasma) and were recruited at hospitals or as outpatients.

B-cell isolation and recombinant mAb production

Discovery and initial characterization of six antibodies in our panel was previously reported (S309 and S304[4,15], S2X35, S2H13 and S2H14[15], and S2E12[8]), and six new antibodies are first described here (S2H97, S2X16, S2H58, S2D106, S2X58, S2X227). Starting from freshly isolated PBMCs or upon cells thawing, B cells were enriched by staining with CD19 PE-Cy7 (BD Bioscience 557835, 1:50) and incubation with anti-PE MicroBeads (Miltenyi Biotec 130-048-801, 1:100), followed by positive selection using LS columns. Enriched B cells were stained with anti-IgM (BioLegend 314508, 1:20), anti-IgD (BD Bioscience 555779, 1:40), anti-CD14 (BD Bioscience 562691, 1:50) and anti-IgA (Southern Biotech 2050-09, 1:400), all PE labeled, and prefusion SARS-CoV-2 S with a biotinylated Avi-tag (in house produced) conjugated to Streptavidin Alexa-Fluor 647 (Life Technologies S21374, 1:40). SARS-CoV-2 S-specific IgG+ memory B cells were sorted by flow cytometry via gating for PE

negative and Alexa-Fluor 647 positive cells. Cells were cultured for the screening of positive supernatants. Antibody VH and VL sequences were obtained by RT-PCR and mAbs were expressed as recombinant human Fab fragment or as IgG1 (G1m3 allotype) carrying the half-life extending M428L/N434S (LS) mutation in the Fc region. ExpiCHO-S cells (Thermo Fisher Scientific) were transiently transfected with heavy and light chain expression vectors as previously described[4]. Affinity purification was performed on ÄKTA Xpress FPLC (Cytiva) operated by UNICORN software version 5.11 (Build 407) using HiTrap Protein A columns (Cytiva) for full length human mAbs and CaptureSelect CH1-XL MiniChrom columns (Thermo Fisher Scientific) for Fab fragments, using PBS as mobile phase. Buffer exchange to the appropriate formulation buffer was performed with a HiTrap Fast desalting column (Cytiva). The final products were sterilized by filtration through 0.22 μm filters and stored at 4ºC.

Using the Database IMGT (http://www.imgt.org), the VH and VL germline gene family and the number of somatic mutations were determined by analyzing the homology of the VH and VL sequences to known human V, D and J genes. Germline-reverted sequences of the VH and VL were constructed using IMGT/V-QUEST. The S2E12 and S2H97 germline-reverted antibodies (G1m17 allotype) were produced by ATUM. S2E12 and S2H97 germline-reverted Fabs were generated by digestion of the corresponding IgGs.

Epitope classes shown in **Figs. 1a and 2g** are defined as in Piccoli et al.[15] Briefly, the classification of these epitope classes results from Octet binning experiments using structurally characterized antibodies, structural insights to define the recognition of open-only RBD and ability of antibodies to interfere with RBD binding to ACE2. In particular, site Ia is accessible only in the open state of RBD and largely overlaps with ACE2 footprint; site Ib is accessible in both open and closed RBD states and overlaps in part with ACE2 footprint; site IIa is in the core RBD (accessible only in the open RBD state) and antibodies binding to this site interfere with binding to ACE2, site IIc is also in the core RBD but targeted by antibodies that do not interfere with binding to ACE2; site IV is fully accessible on both open and closed RBDs and is defined by the footprint of S309 antibody.

Neutralization of authentic SARS-CoV-2 by entry-inhibition assay

Neutralization was determined using SARS-CoV-2-Nluc, an infectious clone of SARS-CoV-2 (based on strain 2019-nCoV/USA_WA1/2020) which encodes nanoluciferase in place of the viral ORF7 and demonstrated comparable growth kinetics to wildtype virus[44]. Vero E6 cells (ATCC, CRL-1586) were seeded into black-walled, clear-bottom 96-well plates at 2×10^4 cells/well and cultured overnight at 37°C. The next day, 9-point 4-fold serial dilutions of mAbs were prepared in infection media (DMEM + 10% FBS). SARS-CoV-2-Nluc was diluted in infection media at a final MOI of 0.01 PFU/cell, added to the mAb dilutions and incubated for 30 minutes at 37°C. Media was removed from the Vero E6 cells, mAb-virus complexes were added and incubated at 37°C for 24 hours. Media was removed from the cells, Nano-Glo luciferase substrate (Promega) was added according to the manufacturer's recommendations, incubated for 10 minutes at room temperature and the luciferase signal was quantified on a VICTOR Nivo plate reader (Perkin Elmer).

404

SARS-CoV-2 spike pseudotyped VSV generation and neutralization assay

Replication defective VSV pseudoviruses[45] expressing SARS-CoV-2 spike protein were generated as previously described[46] with some modifications. Plasmids encoding SARS-CoV-2 spike single-mutant variants were generated by site-directed mutagenesis of the wild-type plasmid, pcDNA3.1(+)-spike-D19[47], and plasmids encoding multiply mutated SARS-CoV-2 variants of concern were generated using a multistep overlap extension PCR protocol[23,48], in which sequential, overlapping fragments were designed to introduce all mutations, which were PCR assembled and cloned into the pcDNA3.1 vector using the Takara In-fusion HD cloning kit following manufacturer's instructions.

Lenti-X 293T (Takara, 632180) cells were seeded in 10-cm dishes at a density of $1x10^5$ cells/cm^2 and the following day transfected with 5 µg of spike expression plasmid with TransIT-Lenti (Mirus, 6600) according to the manufacturer's instructions. For the neutralization assays with variants of concern (Figs. 2d, 3b), Lenti-X 293T cells were seeded in 10-cm dishes at a density of $5x10^6$ cells/cm^2, and transfected the following day with 10 µg of spike expression plasmid. One day post-transfection, cells were infected with VSV (G*ΔG-luciferase) (Kerafast, EH1020-PM) for 1 h, rinsed three times with PBS, then incubated for an additional 24 h in complete media at 37°C. The cell supernatant was clarified by centrifugation, filtered (0.45 µm), aliquoted, and frozen at −80°C.

For VSV pseudovirus neutralization assays, Vero E6 cells (ATCC, CRL-1586) were grown in DMEM supplemented with 10% FBS and seeded into clear bottom white 96 well plates (Costar, 3903) at a density of $2x10^4$ cells per well. The next day, mAbs were serially diluted in pre-warmed complete media, mixed at a 1:1 ratio with pseudovirus and incubated for 1 h at 37°C in round bottom polypropylene plates. Media from cells was aspirated and 50 µL of virus-mAb complexes were added to cells and then incubated for 1 h at 37°C. An additional 100 µL of prewarmed complete media was then added on top of complexes and cells incubated for an additional 16-24 h. Conditions were tested in duplicate wells on each plate and at least six wells per plate contained uninfected, untreated cells (mock) and infected, untreated cells ('no mAb control').

Virus-mAb-containing media was then aspirated from cells and 100 µL of a 1:4 dilution of Bio-glo (Promega, G7940) in PBS was added to cells. For neutralization assays with variants of concern, 50 µL of a 1:2 dilution of SteadyLite Plus (Perkin Elmer) in PBS with $Ca^{2+}Mg^{2+}$ was added to cells in place of Bio-glo. Plates were incubated for 10 min at room temperature and then were analyzed on the Envision plate reader (PerkinElmer), or for variants of concern assays, a Synergy H1 Hybrid Multi-Mode reader (Biotek).

Relative light units (RLUs) for infected wells were subtracted by the average of RLU values for the mock wells (background subtraction) and then normalized to the average of background subtracted "no mAb control" RLU values within each plate. Percent neutralization was calculated by subtracting from 1 the normalized mAb infection condition. Data were analyzed and visualized with Prism (Version 8.4.3). IC_{50} values were calculated from the interpolated value from the log(inhibitor) versus response – variable slope (four parameters) nonlinear regression with an upper constraint of < 100. Neutralization experiments with wildtype SARS-CoV-2 S and single-mutant variants were conducted on three independent days, i.e., biological replicates, where each biological replicate contains a technical duplicate. IC_{50} values across biological replicates are presented as geometric mean. The loss or gain of

445 neutralization potency across spike variants was calculated by dividing the variant IC_{50} by the parental
446 IC_{50} within each biological replicate. Neutralization experiments with SARS-CoV-2 S variants of
447 concern were conducted in biological duplicates, with IC50 values normalized by the corresponding
448 wildtype measurement, and presented as arithmetic mean of the duplicate experiments.
449
450 ### *SARS-CoV-2 spike pseudotyped VSV neutralization on 293T-ACE2 cells*
451 To investigate the effect of ACE2 expression on S2H97 neutralization, Vero E6 cells were seeded at
452 20,000 cells per well in black clear-bottom 96-well plates. 293T-ACE2 cells[31] were seeded at 35,000
453 cells per well in black clear-bottom 96-well plates that had been pre-coated with poly-D-Lysine (Gibco).
454 The next day, SARS-CoV-2 spike-pseudotyped VSV neutralizations with S2E12, S309 and S2H97 were
455 performed as described above. Neutralizations were performed in triplicate wells.
456
457 ### *Sarbecovirus spike pseudotyped VSV neutralization by S2H97*
458 Mammalian expression constructs (pcDNA3.1(+) or pTwist-CMV) encoding the spike proteins from
459 various sarbecoviruses with a C-terminal deletion of 19 amino acids (D19) were synthesized for SARS-
460 CoV-2 (Genbank: QOU99296.1), SARS-CoV-1 Urbani (Genbank: AAP13441.1),
461 hCoV-19/pangolin/Guangdong/1/2019 (GD-Pangolin-CoV, Genbank: QLR06867.1), Pangolin
462 coronavirus Guanxi-2017 (GX-Pangolin-CoV, Genbank: QIA48623.1), and bat sarbecovirus WIV1
463 (WIV1, Genbank: AGZ48828.1). Lenti-X 293T cells (Takara, 632180) were seeded in 15 cm dishes
464 such that the cells would reach 80% confluency after culturing overnight. The following day, cells were
465 transfected using TransIT-Lenti (Mirus, 6600) according to the manufacturer's instructions. One day
466 post-transfection, cells were infected with VSV (G*ΔG-luciferase) (Kerafast, EH1020-PM). The
467 supernatant containing sarbecovirus pseudotyped VSV was collected 2 days post-transfection,
468 centrifuged at $1000 \times g$ for 5 minutes, aliquoted and frozen at $-80°C$.
469   For neutralization assays, cells supporting robust pseudovirus infection were seeded into clear
470 bottom white-walled 96-well plates at 20,000 cells/well in 100 μL culture media. Vero E6 cells were
471 used for VSV-SARS-CoV-2, VSV-SARS-CoV-1, and VSV-GD-Pangolin-CoV. BHK-21 cells (ATCC,
472 CCL-10) stably expressing ACE2 were used for VSV-GX-Pangolin-CoV and VSV-WIV1. After
473 culturing cells overnight, 1:3 serial dilutions of antibody were prepared in DMEM in triplicate.
474 Pseudovirus was diluted in DMEM and added to each antibody dilution such that the final dilution of
475 pseudovirus was 1:20. Pseudovirus:antibody mixtures were incubated for 1 hour at 37°C. Media was
476 removed from the cells and 50 μL of pseudovirus:antibody mixtures were added. One hour post-
477 infection, 50 μL of culture media was added to wells containing pseudovirus:antibody mixtures and
478 incubated overnight at 37°C. Media was then removed and 100 μL of 1:1 diluted DPBS:Bio-Glo
479 (Promega, G7940) luciferase substrate was added to each well. The plate was shaken at 300 RPM at
480 room temperature for 10 minutes after which RLUs were read on an EnSight (Perkin Elmer) microplate
481 reader. Percent neutralization was determined by first subtracting the mean background (cells with
482 luciferase substrate alone) RLU values of 6 wells per plate for all data points. Percent neutralization for
483 each antibody concentration was calculated relative to no antibody control wells for each plate. Percent
484 neutralization data were analyzed and graphed using Prism (GraphPad, v9.0.1). Absolute IC_{50} values
485 were calculated by fitting a curve using a non-linear regression model (variable slope, 4 parameters) and

486 values were interpolated from the curve at y=50. The geometric mean from at least two independent
487 experiments was calculated using Excel (Microsoft, Version 16.45).
488
489 *Sarbecovirus spike pseudotyped VSV neutralization by S2E12*
490 Spikes from SARS-CoV-2 (CAD0240757.1), RaTG13 (QHR63300.2), GD-Pangolin (QLR06867.1),
491 GX-Pangolin (QIA48623.1), SARS-CoV-1 Tor2 (YP009825051), WIV1 (AGZ48831.1) and WIV16
492 (ALK02457.1) were used to pseudotype VSV. To produce pseudotyped viruses, HEK293T/17 (ATCC,
493 CRL-11268) seeded in 10 cm dishes in DMEM supplemented with 10% FBS, 1% PenStrep were
494 transfected with plasmids using lipofectamine 2000 (Life Technologies) following manufacturer's
495 instructions. One day post-transfection, cells were infected with VSV (G*ΔG-luciferase) for 2 h and
496 washed four times with DMEM, before adding medium supplemented with anti-VSV-G antibody (I1-
497 mouse hybridoma supernatant at 1:50 dilution, from CRL-2700, ATCC). Pseudotyped particles were
498 harvested 18 h post-inoculation, clarified by centrifugation at 2000×g for 5 min, concentrated 10× with a
499 30 kDa cutoff membrane filter, and stored at −80°C. For S2E12 neutralization experiments, 293T cells
500 stably expressing ACE2 (BEI #NR-52511)[43] in DMEM supplemented with 10% FBS and 1% PenStrep
501 were seeded at 40,000 cells/well in clear-bottom white-walled 96-well plates and cultured overnight at
502 37°C. Twelve 3-fold serial dilutions of S2E12 antibody were prepared in DMEM, and antibody dilutions
503 were mixed 1:1 with pseudotyped VSV in the presence of 1:50 diluted anti-VSV-G antibody. After 45
504 min incubation at 37°C, 40 μL of antibody-virus mixture was added to cells, and 40 μL DMEM was
505 added 2 h post-infection. After 17-20 h, 50 μL One-Glo-EX substrate (Promega) was added to the cells.
506 Cells were incubated in the dark for 5-10 min prior to luminescence reading on a Varioskan LUX plate
507 reader (Thermo Fisher Scientific). Relative luciferase unit values were converted to percentage of
508 neutralization and plotted with a nonlinear regression curve fit in GraphPad Prism. Measurements were
509 performed in duplicate with two independent productions of pseudotyped virus.
510
511 *Recombinant protein production*
512 SARS-CoV-2 RBD WT proteins for SPR binding assays (with N-terminal signal peptide and C-terminal
513 thrombin cleavage site-TwinStrep-8xHis-tag) were expressed in Expi293F (Thermo Fisher Scientific)
514 cells at 37°C and 8% CO_2. Transfections were performed using the ExpiFectamine 293 Transfection Kit
515 (Thermo Fisher Scientific). Cell culture supernatants were collected three days after transfection and
516 supplemented with 10x PBS to a final concentration of 2.5x PBS (342.5 mM NaCl, 6.75 mM KCl and
517 29.75 mM phosphates). SARS-CoV-2 RBDs were purified using 1 or 5 mL HisTALON Superflow
518 cartridges (Takara Bio) and subsequently buffer exchanged into 1x HBS-N buffer (Cytiva) or PBS using
519 a Zeba Spin Desalting (Thermo Fisher Scientific) or HiPrep 26/10 (Cytiva) desalting column.
520   SARS-CoV-2 RBD WT for crystallization (with N-terminal signal peptide and 'ETGT', and C-
521 terminal 8xHis-tag) was expressed similarly as described above in the presence of 10 μM kifunensine.
522 Cell culture supernatant was collected four days after transfection and supplemented with 10x PBS to a
523 final concentration of 2.5x PBS. Protein was purified using a 5 ml HisTALON Superflow cartridge
524 followed by size exclusion chromatography on a Superdex 200 Increase 10/300 GL column (Cytiva)
525 equilibrated in 20 mM Tris-HCl pH 7.5, 150 mM NaCl. For crystallization of the RBD-S2X259-S2H97

526 and RBD-S2E12-S304-S309 Fab complexes, RBD was deglycosylated by overnight incubation with
527 EndoH glycosidase at 4°C.
528   RBDs from other sarbecoviruses for SPR (with N-terminal signal peptide and C-terminal
529 thrombin cleavage site-TwinStrep-8xHis-tag) were expressed in Expi293F cells at 37°C and 8% CO_2.
530 Cells were transfected using PEI MAX (Polysciences) at a DNA:PEI ratio of 1:3.75. Transfected cells
531 were supplemented three days after transfection with 3 g/L glucose (Bioconcept) and 5 g/L soy
532 hydrolysate (Sigma-Aldrich Chemie GmbH). Cell culture supernatant (423 mL) was collected seven
533 days after transfection and supplemented with 47 mL 10x binding buffer (1 M Tris-HCl, 1.5 M NaCl, 20
534 mM EDTA, pH 8.0) and 25 mL BioLock (IBA GmbH) and incubated on ice for 30 min. Proteins were
535 purified using a 5 mL Strep-Tactin XT Superflow high capacity cartridge (IBA GmbH) followed by
536 buffer exchange to PBS using HiPrep 26/10 desalting columns (Cytiva).
537   Prefusion-stabilized SARS-CoV-2 spike proteins for SPR (residues 14-1211, either D614 or
538 D614G), containing the 2P and Furin cleavage site mutations[49] with a mu-phosphatase signal peptide
539 and a C-terminal Avi-8xHis-C-tag or C-terminal 8xHis-Avi-C-tag were expressed in Freestyle 293-F
540 cells (Thermo Fisher Scientific, R79007) at 37°C and 8% CO_2. Transfections were performed using
541 293fectin as a transfection reagent. Cell culture supernatant was collected after three days and purified
542 over a 5 mL C-tag affinity matrix. Elution fractions were concentrated and injected on a Superose 6
543 Increase 10/300 GL column (Cytiva) with 50 mM Tris-HCl pH 8.0 and 200 mM NaCl as running buffer.
544   SARS-CoV-2 HexaPro spike protein for cryoEM analysis was produced in Freestyle 293-F cells
545 grown in suspension using FreeStyle 293 expression medium (Life Technologies) at 37°C in a
546 humidified 8% CO_2 incubator rotating at 130 RPM. The cultures were transfected using PEI (9 µg/mL)
547 with cells grown to a density of 2.5 million cells per mL and cultivated for three days. The supernatants
548 were harvested and cells resuspended for another three days, yielding two harvests. Spike proteins were
549 purified from clarified supernatants using a 5 mL Cobalt affinity column (Cytiva, HiTrap TALON
550 crude), concentrated and flash frozen in a buffer containing 20 mM Tris pH 8.0 and 150 mM NaCl prior
551 to analysis.
552   SARS-CoV-2 S native-like ectodomain trimer for refolding assays was engineered with a mu-
553 phosphatase signal peptide beginning at 14Q, a mutated S1/S2 cleavage site (SGAR), and a TEV
554 cleavage, fold-on trimerization motif, and 8x His tag appended to the C-terminus (K1211). Native-like
555 spike was expressed and purified as described for SARS-CoV-2 HexaPro spike above.
556   Recombinant hACE2 for SPR (residues 19-615 from Uniprot Q9BYF1 with a C-terminal
557 AviTag-10xHis-GGG-tag, and N-terminal signal peptide) was produced by ATUM. Protein was purified
558 via Ni Sepharose resin followed by isolation of the monomeric hACE2 by size exclusion
559 chromatography using a Superdex 200 Increase 10/300 GL column (Cytiva) pre-equilibrated with PBS.
560
561 *SPR binding assays*
562 SPR binding measurements were performed using a Biacore T200 instrument with CM5 sensor chip
563 covalently immobilized with StrepTactin XT to capture recombinant RBD proteins (data in **Fig. 1a** and
564 **Extended Data Fig. 4f,i,l**). Running buffer was Cytiva HBS-EP+ (pH 7.4). All measurements were
565 performed at 25°C. Fab (or hACE2) analyte concentrations were 11, 33, 100, and 300 nM, run as single-
566 cycle kinetics. Double reference-subtracted data were fit to a 1:1 binding model using Biacore T200
567 Evaluation (version 3.1) or Biacore Insight Evaluation (version 2.0.15) software. K_D above 1 µM were

568 determined from fits where Rmax was set as a constant based on results for higher affinity analytes
569 binding to the same RBD at the same surface density. Data are representative of duplicate or triplicate
570 measurements (except measurements with germline Fabs were singleton measurements).
571   To corroborate the SARS-CoV-2 RBD binding measurements, experiments were also performed
572 in two additional formats, both with monovalent analytes (data in **Extended Data Table 1**): (1) Fab
573 binding to SARS-CoV-2 spike ectodomain was measured using CM5 sensor chips immobilized with
574 anti-AviTag pAb (Genscript, A00674-40) for capturing S, other experiment parameters same as above,
575 and (2) RBD binding to IgG was measured using CM5 sensor chips immobilized with anti-human Fc
576 pAb (Southern Biotech, 2014-01) for capturing IgG, with RBD analyte concentrations of 3.1, 12.5, and
577 50 nM, other experiment parameters same as above. Fit results yield an "apparent K_D" for the spike-
578 binding experiments because the kinetics also reflect spike conformational dynamics. Spike ectodomain
579 was D614G with C-terminal 8xHis-Avi-C-tag for all measurements except S2X58 binding was
580 performed with D614 spike with C-terminal Avi-8xHis-C-tag. For the comparison of mature and
581 germline-reverted antibody binding to RaTG13, the data reported are from experiment format (2) with
582 IgG as ligand. These data were fit to a Heterogeneous Ligand model, due to an artifactual kinetic phase
583 with very slow dissociation that often arises when RBD is an analyte; the lower affinity of the two K_Ds
584 reported by the fit is given as the K_D (the two K_Ds are separated by at least one order of magnitude).
585
586 *Deep mutational scanning mutant escape profiling*
587 We used a previously described deep mutational scanning approach[3] to comprehensively identify RBD
588 mutations that escape binding by each antibody. This approach leverages duplicate RBD mutant
589 libraries[26], which contain virtually all of the 3,819 possible amino acid mutations in the background of
590 the Wuhan-Hu-1 RBD sequence. Library variants were previously linked to short identifier barcode
591 sequences and sorted to purge the library of variants that strongly decrease ACE2 binding affinity or
592 expression of folded RBD[3].
593   We first used an isogenic yeast strain expressing the unmutated SARS-CoV-2 RBD and flow
594 cytometry to identify the EC90 of each antibody's binding to yeast-displayed SARS-CoV-2 RBD. We
595 then performed library selections as previously described[3,20], labeling libraries with the EC90
596 concentration of antibody to standardize escape mutation sensitivity across selections. Briefly, libraries
597 of yeast were induced for surface expression, washed, and labeled with the primary antibody for one
598 hour at room temperature. Cells were washed, and secondarily labeled with 1:200 PE-conjugated goat
599 anti-human-IgG antibody (Jackson ImmunoResearch 109-115-098) to label for bound antibody, and
600 1:100 FITC-conjugated chicken anti-Myc-tag (Immunology Consultants Lab, CYMC-45F) to label for
601 RBD surface expression. We prepared controls for setting FACS selection gates by labeling yeast
602 expressing the unmutated SARS-CoV-2 RBD with the same antibody concentration as library selections
603 (1x), 100x reduced antibody concentration to illustrate the effect of mutations with 100x-reduced
604 affinity, and 0 ng/mL antibody to illustrate complete loss of antibody binding. Representative selection
605 gates are shown in **Extended Data Fig. 2b**. Gates were set and sorting performed with FACSDiva
606 software (version 6.1.3). We sorted approximately 7.5×10^6 RBD+ cells per library on a BD FACSAria
607 II, collecting yeast cells from the antibody-escape sort bin (fractions of library falling into antibody
608 escape bin given in **Extended Data Fig. 2c**). Sorted cells were recovered overnight, plasmids were

609 extracted from the pre-sort and antibody-escape populations, and variant-identifier barcode sequences
610 were PCR amplified and sequenced on an Illumina HiSeq 2500[3,26].

611 As previously described[3,20], sequencing counts pre- and post-selection were used to estimate the
612 "escape fraction" for each library variant, which reflects the fraction of yeast expressing a variant that
613 fall into the antibody-escape FACS bin. Briefly, we used the dms_variants package
614 (https://jbloomlab.github.io/dms_variants/, version 0.8.2) to process Illumina sequences into variant
615 counts pre- and post-selection using the barcode/RBD variant lookup table from Starr et al.[26]. We then
616 computed per-variant escape fractions as: $E_v = F \times (n_v^{post} / N_{post}) / (n_v^{pre} / N_{pre})$, where F is the total fraction
617 of the library that escapes antibody binding (Extended Data Fig. 2c), n_v^{post} and n_v^{pre} are the sequencing
618 counts of variant v in the RBD library after and before FACS selection (with a pseudocount of 0.5 added
619 to all counts), and N_{post} and N_{pre} are the total counts of all variants after and before FACS selection. We
620 then applied computational filters to remove variants with low pre-sort sequencing counts or highly
621 deleterious mutations that might cause artefactual antibody escape due to global unfolding or loss of
622 expression of RBD on the cell surface. Specifically, we filtered out variants whose pre-selection
623 sequencing counts were lower than the 99th percentile counts of variants containing premature stop
624 codons, which were largely purged by the prior sorts for RBD expressing and ACE2-binding RBD
625 variants. We also removed variants with ACE2 binding scores < -2.35 or RBD expression scores < -1,
626 and variants containing individual mutations with effects below these thresholds, using the variant- and
627 mutation-level deep mutational scanning measurements of Starr et al.[26]. We also filtered out rare
628 mutations with low coverage in the libraries, retaining mutations that were sampled on at least one
629 single-mutant barcoded variant or at least two multiply-mutated variants in each replicate. Last, to
630 decompose single-mutation escape fractions for each antibody, we implemented global epistasis
631 models[50] using the dms_variants package to estimate the effect of each individual amino acid mutation,
632 exactly as described in ref. [20].

633 Antibody escape selections were conducted in full duplicate using independently generated and
634 assayed SARS-CoV-2 mutant libraries (see correlations in **Extended Data Fig. 2e,f**). The reported
635 escape fractions throughout the paper are the average across the two replicates, and these final per-
636 mutation escape fractions are provided on GitHub: https://github.com/jbloomlab/SARS-CoV-2-
637 RBD_MAP_Vir_mAbs/blob/main/results/supp_data/vir_antibodies_raw_data.csv.   Interactive
638 visualizations of antibody escape maps (https://jbloomlab.github.io/SARS-CoV-2-
639 RBD_MAP_Vir_mAbs) were created using dms-view[51].

640

641 ***Sarbecovirus library binding assays***
642 A curated set of all unique sarbecovirus RBD amino acid sequences was gathered, including the
643 sarbecovirus RBD sequence set reported by Letko et al.[7], along with additional unique RBD sequences
644 among SARS-CoV-1 epidemic strains reported by Song et al.[52], BtKY72[53] and new sarbecovirus
645 sequences RmYN02[54], GD-Pangolin-CoV (consensus RBD reported in Fig. 3a of Lam et al.[55]), and GX-
646 Pangolin-CoV[55] (P2V, ambiguous nucleotide within codon 515 (SARS-CoV-2 spike numbering)
647 resolved to retain F515, which is conserved in all other sarbecoviruses). A list of all RBDs and sequence
648 accession numbers is available on GitHub: https://github.com/jbloomlab/SARSr-CoV_RBD_MAP/blob/
649 main/data/RBD_accessions.csv

650   To define clades of sarbecovirus RBDs, an alignment of amino acid RBD sequences was
651 generated using mafft[56] with gap opening penalty 4.5 (alignment available on GitHub:
652 https://github.com/jbloomlab/SARSr-CoV_RBD_MAP/blob/main/data/RBD_aa_aligned.fasta). The
653 corresponding nucleotide sequence alignment was generated from the amino acid alignment using
654 PAL2NAL[57]. The gene sequence phylogeny was inferred using RAxML version 8.2.12[58], with the
655 GTRGAMMA substitution model and a partition model with separate parameters for first, second, and
656 third codon positions. The Hibecovirus RBD sequence Hp-Zhejiang2013 (Genbank: KF636752) was
657 used as an outgroup for rooting of the sarbecovirus phylogeny.

658   All unique sarbecovirus RBD protein-coding sequences were ordered from IDT, Twist, and
659 Genscript, and cloned into our yeast display vector[26]. Sequences were pooled and appended with
660 downstream 16-nt barcode sequences according to the protocol described in Starr et al.[26]. Long read
661 circular consensus sequences spanning the 16-nt barcode and RBD genotype were gathered on a PacBio
662 Sequel v2.0 and processed exactly as described in Starr et al.[26]. This yielded a barcode:variant lookup
663 table for the sarbecovirus RBD library analogous to that used for SARS-CoV-2 mutant libraries. This
664 table is available on GitHub:
665 https://github.com/jbloomlab/SARSr-CoV_RBD_MAP/blob/main/data/barcode_variant_table.csv.

666   The pooled sarbecovirus RBD library was labeled, sorted, and quantified as described for the
667 SARS-CoV-2 mutant libraries above, except we only sorted ~1 million RBD+ cells due to the reduced
668 library size. Sequencing and quantification of per-variant antibody escape was conducted as described
669 above. Data for the HKU3-8 RBD is not shown, as this RBD did not express in our yeast-display
670 platform. For several antibodies, we performed a secondary experiment, selecting the sarbecovirus RBD
671 library with a more stringent "full escape" gate to select out only variants exhibiting complete loss of
672 binding (**Extended Data Fig. 2b,c**).

673   For follow-up quantitative binding assays, select sarbecovirus RBDs were cloned into the yeast-
674 display platform as isogenic stocks. Binding assays were conducted across a titration series of antibody
675 in 96-well plates, and binding at each antibody concentration (geometric mean fluorescence intensity in
676 the PE channel among RBD+ (FITC+) cells) was determined via flow cytometry and fit to a four-
677 parameter Hill curve to identify the EC50 (midpoint).

678

679 *Analysis of mutations in natural SARS-CoV-2 sequences*
680 All spike sequences on GISAID[59] as of May 2, 2021, were downloaded and aligned via mafft[56].
681 Sequences from non-human origins, sequences with gaps or ambiguous characters in the RBD, and
682 sequences with more than 8 amino acid differences from the Wuhan-Hu-1 reference sequence (Genbank
683 MN908947, residues N331-T531) were removed. We determined mutation frequencies compared to
684 Wuhan-Hu-1 reference from this final alignment of 1,190,241 sequences. We acknowledge all
685 contributors to the GISAID EpiCoV database for their sharing of sequence data. All contributors to
686 GISAID EpiCoV listed at:
687 https://github.com/jbloomlab/SARS-CoV-2-RBD_MAP_Vir_mAbs/blob/main/data/gisaid_hcov-
688 19_acknowledgement_table_2021_03_04.pdf.

689

690 *Quantitative summary metrics of antibody properties*

691 The relative epitope size of an antibody was calculated as the sum of per-mutant escape fractions that
692 are at least five times the global median escape fraction (to minimize the impact of variation in
693 background noise on the summation). For this summation, escape fractions were normalized to the
694 maximum per-mutation escape fraction, to account for slight variation in the largest per-mutation escape
695 fraction measured between selections.

696 The relative escapability of an antibody was calculated the same as relative epitope size, but each
697 mutation was multiplied by two weighting factors scaled from 0 to 1 that reflect the impact of that
698 mutation on ACE2-binding affinity and RBD expression as measured in our prior deep mutational
699 scan[26]. The relationship between weighting factors and mutation effect on each property is shown in
700 **Extended Data Fig. 3a**. Mutations with < –1 effect on either property are effectively zeroed out in the
701 escapability summation. Mutations with effects between –1 and 0 have intermediate weights, and
702 mutations with 0 or positive effects are assigned weight factors of 1.

703 Antibody susceptibility to escape by natural SARS-CoV-2 mutations was calculated as the
704 summed GISAID frequencies of all escape mutations, where escape mutations (all labels in **Extended**
705 **Data Fig. 3c**) are defined as those with escape fraction greater than five times the median escape fraction
706 as above. These summed natural escape frequencies are tabulated in the plot headers in **Extended Data**
707 **Fig. 3c**.

708 The summary breadth of an antibody was calculated from the sarbecovirus RBD library escape
709 selection using the standard gating (**Extended Data Fig. 4b**), only. Although we have various follow-up
710 binding data illustrating reduced affinity binding for some "escaped" sarbecovirus RBDs, these follow-
711 up experiments were not conducted systematically for all antibody/RBD combinations, and therefore
712 would bias breadth estimates. Breadth of binding was calculated as the frequency of all sarbecovirus
713 RBDs that are bound with affinity within the FACS selection gating threshold, weighted by clade
714 representation. Breadth was normalized to give equal representation to each of the four sarbecovirus
715 clades to account for different depth of sampling. Within the SARS-CoV-1 clade, all human 02/03
716 strains and civet + human 03/04 strains were similarly down-weighted to each represent 1/8 of the
717 possible breadth within the SARS-CoV-1 clade (together with the six bat sarbecoviruses in this clade).
718 As an example, breadth for S304 is calculated as [4/4 +([6/6]+[6/6]+5)/8 + 2/2 + 0/21]/4 = 0.72, based
719 on the data shown in Extended Data Fig. 4b.

720

721 *Multidimensional scaling projection of antibody epitopes*
722 Multidimensional scaling projection in Fig. 4 was performed using the Python scikit-learn package. We
723 first computed the similarity and dissimilarity in the sites of escape between each pair of antibodies,
724 exactly as described in Greaney et al.[3], and performed metric multidimensional scaling with two
725 components on the matrix of dissimilarities between all antibody pairs. Antibodies in this layout were
726 colored with pie charts proportional to the total squared site-wise escape that falls into the labeled
727 structural regions (RBM = residues 437 to 508, ACE2 contact defined as 4Å cutoff based on 6M0J
728 crystal structure[60], and core RBD otherwise). In this layout, we included all of our previously published
729 antibodies for which we have performed escape mapping via this same approach. These antibodies and
730 their citations include: S2X259[37]; LY-CoV555[21]; COV2-2196 and COV2-2130[36]; REGN10933,
731 REGN10987, and LY-CoV016[20]; and all other COV2 antibodies and CR3022[3].

For **Fig. 4b-d** and **Extended Data Fig. 7c**, we colored the antibodies within this layout according to various antibody properties. When appropriate, we also colored these previously assayed antibodies, as described below. **Extended Data Fig. 7d** and the scatterplots in **Fig. 4e-g** show the relationships between properties for antibodies specifically in this study (and S2X259) for the most direct comparability.

Antibody neutralization potencies illustrated in **Fig. 4b** incorporate the authentic SARS-CoV-2 neutralization IC50s as reported in this study (**Fig. 1a**), together with the live SARS-CoV-2 neutralization IC50s for the COV2 antibodies reported by Zost et al.[10]. We acknowledge that it is imperfect to compare neutralization potencies reported from different labs on different antibody batches, though in this case, both sets are indeed neutralization potencies with authentic virus. We therefore do not directly compare these two sets of measurements in a quantitative manner, but we do note that their joint inclusion in **Fig. 4b** supports the dichotomy between neutralization potency of core RBD versus RBM antibodies which is supported by either neutralization panel alone.

Sarbecovirus breadth illustrated in **Fig. 4c** incorporates the pan-sarbecovirus breadth measurements reported in the current study together with more limited breadth measurements for antibodies reported in our prior publications. These previously published experiments determined binding within a more restricted sarbecovirus RBD set present in our libraries (SARS-CoV-2, RaTG13, GD-Pangolin, SARS-CoV-1 [Urbani], LYRa11, and WIV1). We calculated breadth from this incomplete sarbecovirus sequence set for comparison, but note that these antibodies are limited to a relative breadth of 0.5 because no RBDs from the Africa/Europe or non-ACE2-utilizing Asia clades were included. However, as with neutralization, inclusion of these antibodies nonetheless emphasizes the core RBD/RBM dichotomy in sarbecovirus breadth established by our primary panel.

For illustrations of epitope size and escapability in **Fig. 4d** and **Extended Data Fig. 7c**, we calculated these quantities for our previously profiled antibodies as described above. We excluded the antibodies profiled in Greaney et al.[3], as these assays were performed on a prior version of our SARS-CoV-2 mutant library that exhibited different quantitative features of absolute escape, complicating its quantitative comparison to extent of escape for antibodies profiled in this and our other studies, which all use the same library.

Structural mappings around the perimeter of **Fig. 4a** were created by mapping total site-wise escape to the b-factor column of PDB structures. Footprints were defined as residues within a 5Å cutoff of antibody heavy atoms. Structures used were those described in this paper, or previously published structures: ACE2-bound RBD (6M0J)[60], CR3022-bound RBD (6W41)[61], REGN10987- and REGN10933-bound RBD (6XDG)[62], CB6- (LY-CoV016) bound RBD (7C01)[63], and S304, S309, and S2H14-bound RBD (7JX3)[15].

RBD ELISA

96 half area well-plates (Corning, 3690) were coated over-night at 4°C with 25 µL of sarbecoviruses RBD proteins at 5 µg/mL in PBS pH 7.2. Plates were blocked with PBS 1% BSA (Sigma-Aldrich, A3059) and subsequently incubated with mAb serial dilutions for 1 h at room temperature. After 4 washing steps with PBS 0.05% Tween 20 (PBS-T) (Sigma-Aldrich, 93773), goat anti-human IgG secondary antibody (Southern Biotech, 2040-04) was added and incubated for 1 h at room temperature.

773 Plates were then washed 4 times with PBS-T and 4-NitroPhenyl phosphate (pNPP, Sigma-Aldrich,
774 71768) substrate added. After 30 min incubation, absorbance at 405 nm was measured by a plate reader
775 (Biotek) and data plotted using Prism GraphPad.
776

777 ***Binding to cell surface expressed sarbecovirus S proteins by flow cytometry***
778 ExpiCHO-S cells were seeded at 6×10^6 cells cells/mL in a volume of 5 mL in a 50 mL bioreactor.
779 Spike coding plasmids were diluted in cold OptiPRO SFM, mixed with ExpiFectamine CHO Reagent
780 (Life Technologies) and added to the cells. Transfected cells were then incubated at 37°C with 8% CO_2
781 with an orbital shaking speed of 120 RPM (orbital diameter of 25 mm) for 42 hours. Transiently
782 transfected ExpiCHO-S cells were harvested and washed two times in wash buffer (PBS 1% BSA, 2
783 mM EDTA). Cells were counted and distributed into round bottom 96-well plates (Corning) and
784 incubated with 10 μg/mL S2H97, S2X35 or S309 mAb. Alexa Fluor647-labelled Goat Anti-Human IgG
785 secondary Ab (Jackson ImmunoResearch 109-607-003) was prepared at 1.5 μg/mL added onto cells
786 after two washing steps. Cells were then washed twice and resuspended in wash buffer for data
787 acquisition on a ZE5 cytometer (Biorad).
788

789 ***Crystallization, data collection, structure determination, and analysis***
790 To form RBD-Fab complexes for crystallization, SARS-CoV-2 RBD was mixed with a 1.3-fold molar
791 excess of each Fab and incubated on ice for 20-60 min. Complexes were purified on a Superdex 200
792 Increase 10/300 GL column (Cytiva) preequilibrated with 20 mM Tris-HCl pH 7.5 and 150 mM NaCl.
793 Crystals of the RBD-Fab complexes were obtained at 20°C by sitting drop vapor diffusion.
794   For the SARS-CoV-2 RBD-S2X35-S309 complex, a total of 200 nL complex at 5.4 mg/mL was
795 mixed with 100 nL mother liquor solution containing 1.85 M Ammonium Sulfate, 0.1 M Tris pH 8.17,
796 0.8% (w/v) polyvinyl alcohol, 1% (v/v) 1-propanol, and 0.01 M HEPES pH 7. Crystals were flash frozen
797 in liquid nitrogen using the mother liquor solution supplemented with 20% glycerol for cryoprotection.
798 Data were collected at Beamline 9-2 of the Stanford Synchrotron Radiation Lightsource facility in
799 Stanford, CA and processed with the XDS software package (version Jan 31, 2020)[64] to 1.83 Å in space
800 group C222. The RBD-S2X35-S309 Fab complex structure was solved by molecular replacement using
801 phaser[65] from a starting model consisting of RBD-S309 Fab (PDB ID: 7JX3) and a homology model for
802 the S2X35 Fab built using the Molecular Operating Environment (MOE) software package from the
803 Chemical Computing Group (https://www.chemcomp.com).
804   For the SARS-CoV-2-RBD-S2H97-S2X259 Fab complex, 200 nL complex at 5.7 mg/mL were
805 mixed with 200 nL mother liquor solution containing 0.12 M Monosaccharides mix, 20% (v/v) Ethylene
806 glycol, 10% (w/v) PEG 8000, 0.1 M Tris (base)/bicine pH 8.5, 0.02 M Sodium chloride, 0.01 M MES
807 pH 6 and 3% (v/v) Jeffamine ED-2003. Crystals were flash frozen in liquid nitrogen. Data were
808 collected at Beamline 9-2 of the Stanford Synchrotron Radiation Lightsource facility in Stanford, CA.
809 Data were processed with the XDS software package (version Jan 31, 2020)[64] for a final dataset of 2.65
810 Å in space group P2$_1$. The RBD-S2H97-S2X259 Fab complex structure was solved by molecular
811 replacement using phaser from a starting model consisting of SARS-CoV-2 RBD (PDB ID: 7JX3) and
812 homology models for the S2H97 and S2X259 Fabs built using the MOE software package.

813   For the SARS-CoV-2-RBD-S2E12-S304-S309 Fab complex, 200 nL complex at 4.5 mg/mL

814   were mixed with 100 nL of 0.09 M Phosphate/Citrate pH 5.5, 27% (v/v) PEG Smear Low, 4% (v/v)

815   Polypropylene glycol 400 and 0.02 M Imidazole pH 7 or 100 nL of 0.09 M Phosphate/Citrate pH 5.5,

816   27% (v/v) PEG Smear Low, 0.01 M Potassium/sodium phosphate pH 7, 1% (v/v) PPGBA 230 and 1.5%

817   (v/v) PPGBA 400. Crystals were flash frozen in liquid nitrogen. Data were collected at the Molecular

818   Biology Consortium beamline 4.2.2 at the Advanced Light Source synchrotron facility in Berkeley, CA.

819   Datasets from two crystals from the two conditions were individually processed and then merged with

820   the XDS software package (version Jan 31, 2020)[64] for a final dataset of 2.93 Å in space group I4$_1$22.

821   The RBD-S2E12-S304-S309 Fab complex structure was solved by molecular replacement using phaser

822   from starting models consisting of RBD-S304-S309 Fab (PDB ID: 7JX3) and S2E12 (PDB ID: 7K3Q).

823   For all structures, several subsequent rounds of model building and refinement were performed

824   using Coot (version 0.9.5)[66], ISOLDE (ChimeraX version 1.1/ISOLDE version 1.1)[67], Refmac5 (version

825   5.8.0267)[68], and MOE (version 2019.0102) (https://www.chemcomp.com), to arrive at the final models.

826   For all complexes, epitopes on the RBD protein were determined by identifying all RBD residues within

827   a 5.0 Å distance from any Fab atoms. The analysis was performed using the MOE software package and

828   the results were manually confirmed.

829

830   ***Cryo-electron microscopy***

831   SARS-CoV-2 HexaPro S[69] at 1.2 mg/mL was incubated with 1.2 fold molar excess of recombinantly

832   purified S2D106 or S2H97 at 4°C before application onto a freshly glow discharged 2.0/2.0 UltrAuFoil

833   grid (200 mesh). Plunge freezing used a vitrobot MarkIV (Thermo Fisher Scientific) using a blot force

834   of 0 and 6.5 second blot time at 100% humidity and 23°C.

835   For the S/S2D106 data set, Data were acquired using an FEI Titan Krios transmission electron

836   microscope operated at 300 kV and equipped with a Gatan K2 Summit direct detector and Gatan

837   Quantum GIF energy filter, operated in zero-loss mode with a slit width of 20 eV. Automated data

838   collection was carried out using Leginon[70] at a nominal magnification of 130,000x with a pixel size of

839   0.525 Å. The dose rate was adjusted to 8 counts/pixel/s, and each movie was acquired in super-

840   resolution mode fractionated in 50 frames of 200 ms. 2,166 micrographs were collected with a defocus

841   range between -0.5 and -2.5 μm. Movie frame alignment, estimation of the microscope contrast-transfer

842   function parameters, particle picking, and extraction were carried out using Warp[71]. Particle images were

843   extracted with a box size of 800 binned to 400 pixels^2 yielding a pixel size of 1.05 Å.

844   For the S/S2H97 data set, data were acquired on an FEI Glacios transmission electron

845   microscope operated at 200 kV equipped with a Gatan K2 Summit direct detector. Automated data

846   collection was carried out using Leginon[70] at a nominal magnification of 36,000x with a pixel size of

847   1.16 Å. The dose rate was adjusted to 8 counts/pixel/s, and each movie was acquired in counting mode

848   fractionated in 50 frames of 200 ms. 3,138 micrographs were collected in a single session with a defocus

849   range comprised between -0.5 and -3.0 μm. Preprocessing was performed using Warp[71] and particle

850   images were extracted with a box size of 400 pixels^2.

851   For the S/S2D106 and S/S2H97 datasets, two rounds of reference-free 2D classification were

852   performed using CryoSPARC to select well-defined particle images[72]. These selected particles were

853   subjected to two rounds of 3D classification with 50 iterations each (angular sampling 7.5° for 25

854   iterations and 1.8° with local search for 25 iterations), using our previously reported closed SARS-CoV-

855 2 S structure as initial model[49] (PDB 6VXX) in Relion[73]. 3D refinements were carried out using non-
856 uniform refinement[74] along with per-particle defocus refinement in CryoSPARC. Selected particle
857 images were subjected to the Bayesian polishing procedure[75] implemented in Relion3.0 before
858 performing another round of non-uniform refinement in CryoSPARC followed by per-particle defocus
859 refinement and again non-uniform refinement.

860   To further improve the density of the S2D106 Fab, the particles were then subjected to focus 3D
861 classification without refining angles and shifts using a soft mask on RBD and Fab variable domains
862 with a tau value of 60 in Relion. Particles belonging to classes with the best resolved local density were
863 selected and subject to local refinement using CryoSPARC. Local resolution estimation, filtering, and
864 sharpening were carried out using CryoSPARC. Reported resolutions are based on the gold-standard
865 Fourier shell correlation (FSC) of 0.143 criterion and Fourier shell correlation curves were corrected for
866 the effects of soft masking by high-resolution noise substitution[76]. UCSF Chimera[77] and Coot[78] were
867 used to fit atomic models into the cryoEM maps. Spike-RBD/S2D106 Fab model was refined and
868 relaxed using Rosetta using sharpened and unsharpened maps[79].

S2H97-induced spike refolding

871 10 μM native-like SARS-CoV-2 S was incubated with 13 μM S2H97 Fab for 1 hour at room
872 temperature. Samples were diluted to 0.01 mg/mL immediately prior to adsorption to glow-discharged
873 carbon-coated copper grids for ~30 sec prior to a 2% uranyl formate staining. Micrographs were
874 recorded using the Leginon software[70] on a 120 kV FEI Tecnai G2 Spirit with a Gatan Ultrascan 4000
875 4k x 4k CCD camera at 67,000 nominal magnification. The defocus ranged from -1.0 to -2.0 μm and the
876 pixel size was 1.6 Å.

Cell-surface antibody-mediated S1 shedding

879 CHO-K1 cells stably expressing the prototypic SARS-CoV-2 spike protein were harvested, washed in
880 wash buffer (PBS + 1% BSA, 2 mM EDTA) and resuspended in PBS. 90,000 cells per well were
881 dispensed into round bottom 96-well plates (Corning), and treated with 10 μg/mL TPCK-Trypsin
882 (Worthington Biochem) for 30 min at 37°C. Cells were washed and incubated with 15 μg/mL antibody
883 across 5, 30, 60, 120, and 180 min timepoints at 37°C. Cells were washed with ice-cold wash buffer, and
884 stained with 1.5 μg/mL Alexa Fluor647-conjugated goat anti-human IgG secondary antibody (Jackson
885 Immunoresearch) for 30 min on ice in the dark. Cells were washed twice with cold wash buffer and
886 analyzed using a ZE5 cytometer (Biorad) with acquisition chamber at 4°C. Binding at each time point
887 was measured as mean fluorescence intensity (MFI), normalized to the MFI at the 5 min labeling time
888 point. Data was analyzed and plotted using GraphPad Prism v. 9.0.1.

Cell-cell fusion of CHO-S cells

891 Cell-cell fusion between S-expressing CHO-K1 cells was performed as described by Lempp et al.[31].
892 CHO-K1 cells stably expressing the prototypic SARS-CoV-2 spike protein were seeded in 96-well
893 plates (Thermo Fisher Scientific) at 12,500 cells/well. The following day, antibody and nuclei marker
894 Hoechst (final dilution 1:1000) were added to cells and incubated for 24 h. Cell-cell fusion was
895 visualized using the Cytation 5 Imager (BioTek), and an object detection protocol was used to detect

nuclei and measure their size. The nuclei of fused cells (syncytia) are aggregated at the center of the syncytia and recognized as a uniquely large object that is gated according to its size. To quantify cell-cell fusion, we report the area of objects in fused cells divided by the total area of all objects, multiplied by 100 to represent as a percentage.

Antibody blockade of RBD binding to ACE2

ACE2 blockade ELISA was performed as described by Piccoli et al.[15]. Unlabeled antibodies were serially diluted, mixed with RBD mouse Fc-tagged antigen (Sino Biological, final concentration 20 ng/mL) and incubated for 30 min at 37°C. The mix was added for 30 min to ELISA 96-well plates (Corning) pre-coated overnight at 4°C with 2 µg/mL human ACE2 in PBS. Plates were washed and RBD binding was revealed using secondary goat anti-mouse IgG (Southern Biotech 1030-04). After washing, pNPP substrate was added and plates were read at 405 nm. The percentage of inhibition was calculated as: (1 − (OD sample − OD neg ctrl)/(OD pos ctrl − OD neg ctrl)]) x 100.

Inhibition of spike-mediated cell-to-cell fusion

Cell-to-cell fusion inhibition assays were performed as described by McCallum et al.[80]. Vero E6 cells were seeded in 96 well plates at 15,000 cells per well in 70 mL DMEM with high glucose and 2.4% FBS (Hyclone). After 16 h at 37°C with 8% CO2, the cells were transfected as follows: for 10 wells, 0.57 mg plasmid SARS-CoV-2-S-D19_pcDNA3.1 was mixed with 1.68 mL X-tremeGENE HP in 30 mL OPTIMEM. After 15 min incubation, the mixture was diluted 1:10 in DMEM medium and 30 mL was added per well. 4-fold antibody serial dilutions were prepared and added to the cells, with a starting concentration of 20 µg/mL. The following day, 30 µL 5X concentrated DRAQ5 in DMEM was added per well and incubated for 2 h at 37°C. Nine images of each well were acquired with a Cytation 5 equipment for analysis.

S2H97 prophylactic protection in Syrian hamsters

We used a validated SARS-CoV-2 Syrian Golden hamster model of infection[81,82] to test S2H97 prophylactic efficacy. Experiments were performed in the high-containment A3 and BSL3+ facilities of the KU Leuven Rega Institute (3CAPS) under licenses AMV 30112018 SBB 219 2018 0892 and AMV 23102017 SBB 219 20170589 according to institutional guidelines.

Syrian hamsters (*Mesocricetus auratus*) were purchased from Janvier Laboratories. Hamsters were housed per two in ventilated isolator cages (IsoCage N Biocontainment System, Tecniplast) with ad libitum access to food, water, and cage enrichment (wood block). Housing conditions and experimental procedures were approved by the ethical committee of animal experimentation of KU Leuven (license P065-2020). Sample sizes of 6 hamsters was determined in order to have a significant difference of at least 1 log viral RNA level (effect size d=2.004) between control and treatment groups, by using a 2-tail t-test with 80% power and an alpha of 0.05, calculated with G*Power 3.1 software. 6-10-week-old female hamsters were randomized for administration of 25 mg/kg S2H97 antibody or 20 mg/kg human isotype control via intraperitoneal injection. Approximately 5 h before infection, animals were anesthetized with isoflurane to allow collection of a blood sample from the jugular vein to be used for antibody quantification. Forty-eight hours post antibody injection, hamsters were infected

937 intranasally with 1.89×10^6 TCID$_{50}$ SARS-CoV-2 virus in 50 μL inoculum. The challenge virus was a
938 SARS-CoV-2 Wuhan isolate from February, 2020 (EPI_ISL_407976), passaged on Vero E6 cells.
939 Passage 6 stock titer was determined by end-point dilution on Vero E6 cells by the Reed and Muench
940 method[83], expressed as 50% tissue culture infectious dose (TCID$_{50}$).

941   Hamsters were monitored for appearance, behavior, and weight. At day 4 post-infection,
942 hamsters were euthanized by intraperitoneal injection of 500 μL Dolethal (200 mg/mL sodium
943 pentobarbital, Vétoquinol SA). Lungs were collected, homogenized via bead disruption (Precellys) in
944 350 μL RLT buffer (RNeasy Mini kit, Qiagen) and centrifuged (10,000 rpm, 5 min, 4°C) to pellet cell
945 debris. RNA was extracted using a NucleoSpin kit (Macherey-Nagel) according to manufacturer
946 instructions. RT-qPCR was performed on a LightCycler96 platform (Roche) using the iTaq Universal
947 Probes One-Step RT-qPCR kit (BioRad) with N2 primers and probes targeting the nucleocapsid[81].
948 Standards of SARS-CoV-2 cDNA (IDT) were used to express viral genome copies per mg tissue. To
949 quantify infectious SARS-CoV-2 particles, endpoint titrations were performed on confluent Vero E6
950 cells in 96-well plates. Viral titers were calculated as above, and were expressed as TCID$_{50}$ per mg
951 tissue. The circulating antibody levels were measured by Mesoscale bridging ELISA, using an anti-
952 human LS mutation mAb as a capture and anti-human CH2 mAb as detection. Technicians performing
953 RNA, virus, and antibody quantification were blinded to the treatment groups of processed samples.
954 RNA and viral levels were compared between treatment and control via 2-tailed Mann-Whitney test,
955 excluding the two treatment animals with undetectable S2H97 levels at time of viral challenge.

956

957 *Blockade of binding serology competition assays*
958 Sera blockade of antibody binding was performed as described in Piccoli et al.[15]. Briefly, human IgG1
959 antibodies were biotinylated using the EZ-link NHS-PEO solid phase biotinylation kit (Pierce). Each
960 labeled antibody was tested for binding to RBD by ELISA, and a concentration for each antibody
961 competition experiment was selected to achieve 80% maximal binding (EC$_{80}$). ELISA 96-well plates
962 (Corning) were pre-coated overnight at 4°C with 1 μg/mL of mouse Fc-tagged RBD antigen (Sino
963 Biological) in PBS. Unlabeled sera/plasma were serially diluted and added to ELISA plates for 30 min,
964 followed by addition of biotinylated anti-RBD antibody at its EC$_{80}$ concentration. After 30 min
965 incubation, plates were washed and antibody binding was detected using alkaline phosphatase-
966 conjugated streptavidin (Jackson ImmunoResearch). Plates were washed, pNPP substrate (Sigma-
967 Aldrich) was added, and plates were read at 405 nm. The percentage of inhibition of antibody binding
968 was calculated as: $(1 - (OD_{sample} - OD_{neg\ ctrl}) / (OD_{pos\ ctrl} - OD_{neg\ ctrl})) \times 100$.

969

970 *Selection of VSV-SARS-CoV-2 monoclonal antibody resistance mutants (MARMS)*
971 VSV-SARS-CoV-2 S chimera was used to select for SARS-CoV-2 S monoclonal antibody resistant
972 mutants (MARMS) as previously described[1,84]. Briefly, MARMS were recovered by plaque isolation on
973 Vero E6 cells (ATCC, CRL-1586) with the indicated mAb in the overlay. The concentration of mAb in
974 the overlay was determined by neutralization assays at a multiplicity of infection (MOI) of 100. Escape
975 clones were plaque-purified on Vero cells (ATCC, CCL-81) in the presence of mAb, and plaques in
976 agarose plugs were amplified on MA104 cells (Gift from Harry Greenberg) with the mAb present in the
977 medium. Viral stocks were amplified on MA104 cells at an MOI of 0.01 in Medium 199 containing 2%

978 FBS and 20 mM HEPES pH 7.7 (Millipore Sigma) at 34°C. Viral supernatants were harvested upon
979 extensive cytopathic effect and clarified of cell debris by centrifugation at 1,000 x g for 5 min. Aliquots
980 were maintained at -80°C. Viral RNA was extracted from VSV-SARS-CoV-2 mutant viruses using
981 RNeasy Mini kit (Qiagen), and S was amplified using OneStep RT-PCR Kit (Qiagen). The mutations
982 were identified by Sanger sequencing (GENEWIZ). Their resistance was verified by subsequent virus
983 infection in the presence or absence of antibody. Briefly, Vero cells were seeded into 12 well plates for
984 overnight. The virus was serially diluted using DMEM and cells were infected at 37°C for 1 h. Cells
985 were cultured with an agarose overlay in the presence or absence of mAb at 34°C for 2 days. Plates were
986 scanned on a biomolecular imager and expression of eGFP is shown at 48 h post-infection. The S2X58-
987 selected mutation S494L is not shown in **Fig. 3a**, as its effect on RBD expression was below the deep
988 mutational scanning computational filter.
989
990 *Viral replication fitness assays*
991 Vero E6 cells (ATCC, CRL-1586) were seeded at 1×10^6 cells per well in 6-well plates. Cells were
992 infected with multiplicity of infection (MOI) of 0.02, with WT and four mutant VSV-SARS-CoV-2 S
993 chimeras mixed at equal (0.20) frequencies. Following 1 h incubation, cell monolayers were washed
994 three times with HBBS and cultures were incubated for 72 h in humidified incubators at 34°C. To
995 passage the progeny viruses, virus mixture was continuously passaged four times in Vero E6 cells at
996 MOI of 0.02. Cellular RNA samples from each passages were extracted using RNeasy Mini kit
997 (QIAGEN) and subjected to next-generation sequencing as described previously to confirm the
998 introduction and frequency of substitutions[84].
999
1000 *Molecular dynamics simulations*
1001 Full details of molecular dynamics workflow and analysis are available on GitHub:
1002 https://github.com/choderalab/rbd-ab-contact-analysis. The RBD:S309 complex was constructed from
1003 PDB ID 7JX3 (Chains A, B, and R). 7JX3 was first refined using ISOLDE[67]. Refinement included
1004 adjusting several rotamers, flipping several peptide bonds, fixing several weakly resolved waters, and
1005 building in a missing four-residue-long loop. Though the N343 glycan N-Acetylglucosamine (NAG)
1006 was present in 7JX3, ISOLDE was used to construct a complex glycan at N343. The full glycosylation
1007 pattern was determined from Shajahan et al.[85] and Watanabe et al.[86]. The glycan structure used for N343
1008 (FA2G2) corresponds to the most stable conformer obtained from multi microsecond molecular
1009 dynamics (MD) simulations of cumulative sampling[87]. The base NAG residue in FA2G2 was aligned to
1010 the corresponding NAG stub in the RBD:S309 model and any resulting clashes were refined in ISOLDE.
1011 The same process was repeated for the RBD:S2H97 crystal structure.
1012   The refined glycosylated RBD:S309 and RBD:S2H97 complexes were prepared for simulation
1013 using tleap from AmberTools20[88]. All relevant disulfide bridges and covalent connections in glycan
1014 structures were specified. The glycosylated proteins were parameterized with the Amber ff14SB[89] and
1015 GLYCAM_06j-1[90] force fields. The systems were solvated using the TIP3P rigid water model[91] in a
1016 truncated octahedral box with 2.2 nm solvent padding on all sides. The solvent box's shape and size
1017 were chosen to prevent the protein complex from interacting with its periodic image. The solvated
1018 systems were then neutralized with 0.15 M NaCl using the Li/Merz ion parameters of monovalent ions

1019 for the TIP3P water model (12-6 normal usage set)[92]. Virtual bonds were added across chains that should
1020 be imaged together to aid the post-processing of trajectories.

1021   Each system was energy-minimized with an energy tolerance of 10 kJ mol^{-1} and equilibrated five
1022 times independently using the OpenMMTools 0.20.0 (https://github.com/choderalab/openmmtools)
1023 BAOAB Langevin integrator[93] for 20 ns in the NPT (p=1 atm, T = 310 K) ensemble with a timestep of
1024 4.0 femtoseconds, a collision rate of 1.0 picoseconds^{-1}, and a relative constraint tolerance of 1×10^{-5}.
1025 Hydrogen atom masses were set to 4.0 amu by transferring mass from connected heavy atoms, bonds to
1026 hydrogen were constrained, and center of mass motion was not removed. Pressure was controlled by a
1027 molecular-scaling Monte Carlo barostat with an update interval of 25 steps. Non-bonded interactions
1028 were treated with the Particle Mesh Ewald method[94] using a real-space cutoff of 1.0 nm and the
1029 OpenMM default relative error tolerance of 0.0005, with grid spacing selected automatically. The
1030 simulations were subsequently packaged to seed for production simulation on Folding@home[95,96].
1031 Default parameters were used unless noted otherwise.

1032   The equilibrated structures (five per complex) were used to initiate parallel distributed MD
1033 simulations on Folding@home[95,96]. Simulations were run with OpenMM 7.4.2 (compiled into
1034 Folding@home core22 0.0.13). Production simulations used the same Langevin integrator as the NPT
1035 equilibration described above. 5000 and 4985 independent MD simulations were generated on
1036 Folding@home for RBD:S309 and RBD:S2H97, respectively. Conformational snapshots (frames) were
1037 stored at an interval of 1 ns/frame for subsequent analysis. The final datasets contained 1.1 ms and 623.7
1038 μs of aggregate simulation time for RBD:S309 and RBD:S2H97, respectively. This trajectory dataset
1039 (without solvent) are available at the MolSSI COVID-19 Molecular Structure and Therapeutics Hub:
1040 https://covid.molssi.org//simulations/#foldinghome-simulations-of-the-sars-cov-2-spike-rbd-bound-to-
1041 monoclonal-antibody-s309 and https://covid.molssi.org//simulations/#foldinghome-simulations-of-the-
1042 sars-cov-2-spike-rbd-bound-to-monoclonal-antibody-s2h97.

1043   The first 100 ns of each trajectory was discarded (to allow relaxation away from the crystal
1044 structure), yielding total simulation times of 644.3 and 262.9 μs used for analysis of RBD:S309 and
1045 RBD:S2H97 systems, respectively. All trajectories had solute structures aligned to their first frame and
1046 centered using MDTraj[97]. Residues were considered to be at the interface if they were within 10 Å of
1047 any antibody Fab / RBD residue (with the exception of RBD N343 glycans, where all glycan residues
1048 were considered). The minimum distance of heavy atoms between every pair of interface residues was
1049 computed for every frame (1 ns) using MDAnalysis[98,99]. A close contact was counted if the minimum
1050 distance between a residue pair was below 3.5 Å (if one of the residues was hydrophobic, a 4.5 Å cutoff
1051 was used). The contribution of each RBD residue to close contacts was calculated as a percentage by
1052 summation of the number of close contacts for a particular RBD residue and normalizing by the total
1053 number of close contact interactions over all frames of each simulation.

1054

Materials Availability

1057 - The SARS-CoV-2 RBD mutant libraries (#1000000172) and unmutated parental plasmid
1058 (#166782) are available on Addgene

1059 • Other materials generated in this study will be made available on request and may require a
1060   material transfer agreement
1061

1062 **Data Availability**
1063 • Interactive escape maps and structural visualizations can be found at: https://jbloomlab.github.io/
1064   SARS-CoV-2-RBD_MAP_Vir_mAbs/
1065 • Raw Illumina sequencing data from deep mutational scanning experiments are available on
1066   NCBI SRA, BioSample SAMN18315604 (SARS-CoV-2 mutant selection data) and BioSample
1067   SAMN18316011 (sarbecovirus RBD selection data).
1068 • PacBio sequencing data used to link N16 barcodes to sarbecovirus RBD variant are available on
1069   NCBI SRA, BioSample SAMN18316101.
1070 • Complete table of deep mutational scanning antibody escape fractions is provided on GitHub:
1071   https://github.com/jbloomlab/SARS-CoV-2-RBD_MAP_Vir_mAbs/blob/main/results/
1072   supp_data/all_antibodies_raw_data.csv. This table includes both antibodies first described in this
1073   study (Fig. 1b,c), and all other antibody selections that were re-processed to generate Fig. 4a.
1074 • The X-ray structure data and model has been deposited with accession code PDB 7R6W for
1075   RBD-S2X35-S309, PDB 7M7W for RBD-S2H97-S2X259 and PDB 7R6X for RBD-S2E12-
1076   S304-S309.
1077 • CryoEM structure data and model are available with accession codes EMD-24300 for S/S2D106,
1078   EMD-24299 and PDB 7R7N for the S/S2D106 local refinement, and EMD-24301 for S/S2H97
1079 • The raw and processed molecular dynamics trajectory data are available at the MolSSI COVID-
1080   19   Molecular   Structure   and   Therapeutics   Hub:
1081   https://covid.molssi.org//simulations/#foldinghome-simulations-of-the-sars-cov-2-spike-rbd-
1082   bound-to-monoclonal-antibody-s309   and   https://covid.molssi.org//simulations/#foldinghome-
1083   simulations-of-the-sars-cov-2-spike-rbd-bound-to-monoclonal-antibody-s2h97
1084 • All other datasets generated during and/or analyzed during the current study are available from
1085   the corresponding author on reasonable request
1086

1087 **Code Availability**
1088 • Repository containing all code, analysis, and summary notebooks for the analysis of the SARS-
1089   CoV-2   deep   mutational   scanning   escape   selections   available   on   GitHub:
1090   https://github.com/jbloomlab/SARS-CoV-2-RBD_MAP_Vir_mAbs
1091 • Repository containing code and analysis of the sarbecovirus RBD library binding experiments
1092   available on GitHub: https://github.com/jbloomlab/SARSr-CoV_RBD_MAP
1093 • Repository containing code and analysis of molecular dynamics simulations is available on
1094   GitHub: https://github.com/choderalab/rbd-ab-contact-analysis
1095
1096
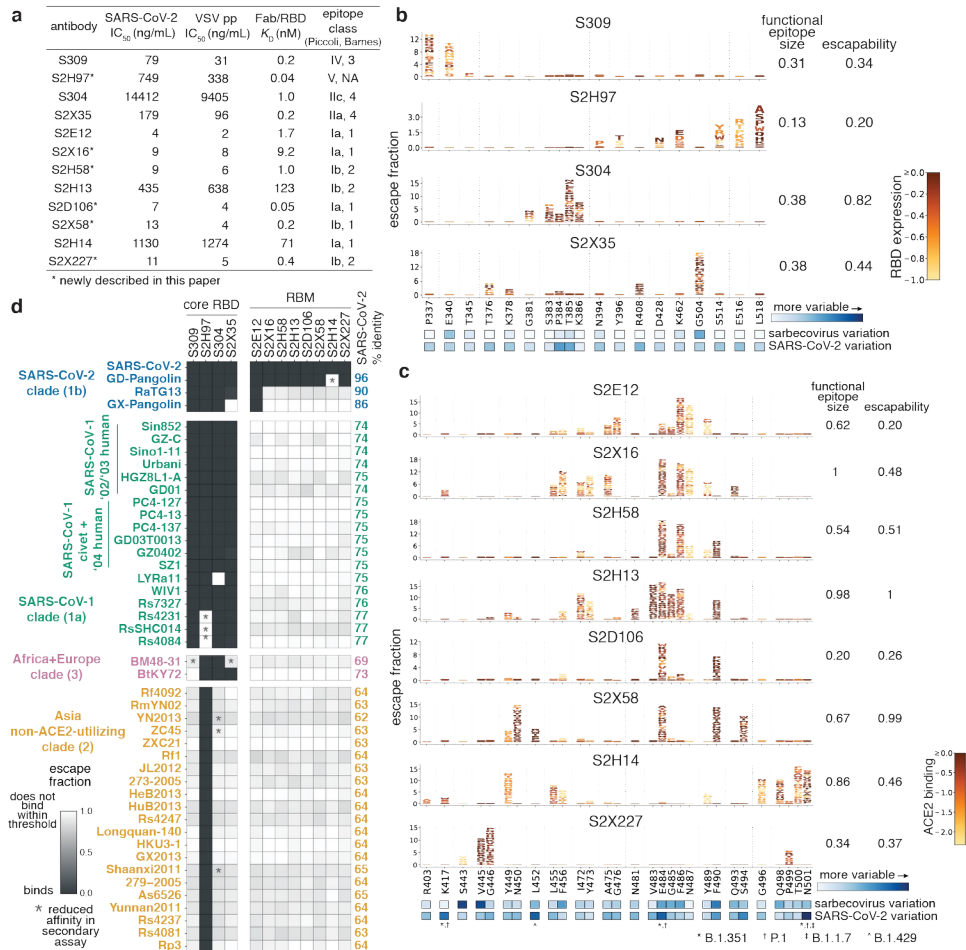
Fig. 1. Potency, escapability, and breadth of a panel of RBD antibodies. **a**, SARS-CoV-2 neutralization potency (authentic virus [$n=3$] and spike-pseudotyped VSV particles [$n = 3$ to 8] on Vero E6 cells), Fab:RBD binding affinities measured by SPR [$n = 2$ to 4], and epitope classifications. Additional details in Extended Data Table 1. **b,c**, Deep mutational scanning maps of mutations that escape binding by antibodies targeting the core RBD (**b**) or the receptor-binding motif (**c**). Letter height indicates that mutation's strength of escape from antibody binding. Letters colored by effect on folded RBD expression (**b**) or ACE2 binding affinity (**c**)[26]. Relative "functional epitope size" and "escapability" are tabulated at right, scaling from 0 (no escape mutations) to 1 (largest epitope/most escapable antibody). Heatmaps, bottom, illustrate variability among sarbecovirus or SARS-CoV-2 sequences. **d**, Antibody binding to a pan-sarbecovirus RBD panel. Heatmap illustrates binding from FACS-based selections (scale bar, bottom left). Asterisks, reduced-affinity binding in secondary binding assays (Extended Data Fig. 4a-f).
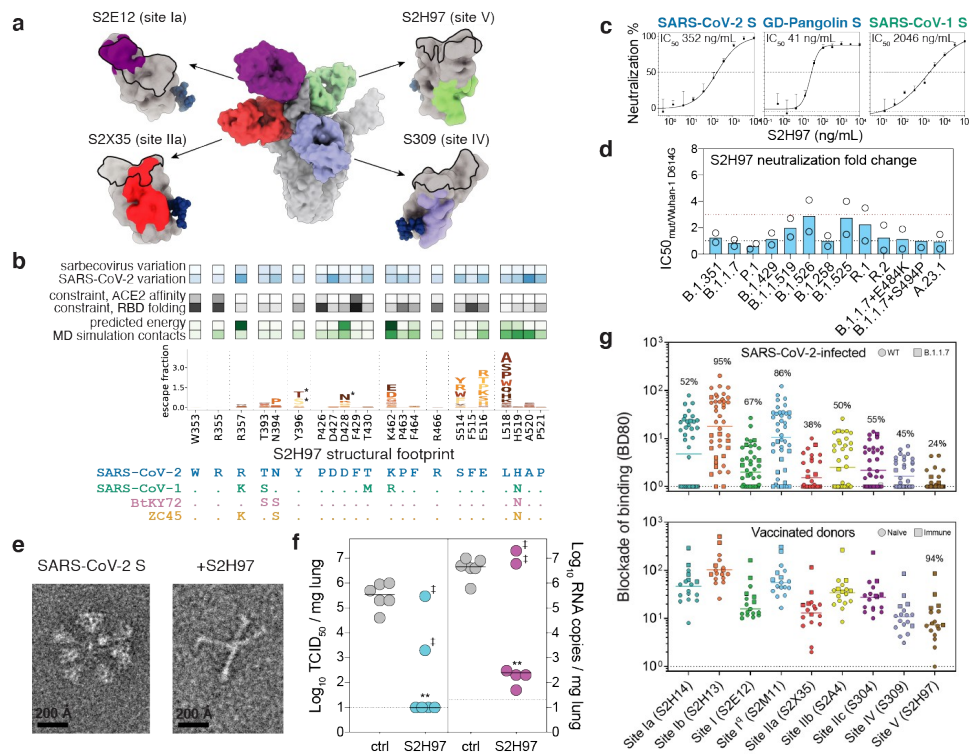
Fig. 2. The pan-sarbecovirus S2H97 antibody. a, Composite model of the SARS-CoV-2 trimer with cross-reactive antibodies. Epitopes recognized by each Fab are shown as colored surface and ACE2 footprint as a black outline. **b**, Integrative features of the S2H97 structural footprint (5 Å cutoff). Heatmaps illustrate evolutionary variability (blue), functional constraint from prior deep mutational scans (gray), and energetic contribution to binding from the static crystal structure or molecular dynamics simulation (green). Logoplot as in Fig. 1b. Asterisk, introduction of N-linked glycosylation motifs. **c,** S2H97 breadth of neutralization (spike-pseudotyped VSV on Vero E6 cells). Curves representative of at least two independent experiments. Points represent means, error bars standard deviation from three technical replicates, and IC50 geometric mean of experiments. **d**, S2H97 neutralization of SARS-CoV-2 variants (Extended Data Fig. 1d; spike-pseudotyped VSV on Vero E6 cells). Points represent individual measurements and bar mean fold-change in neutralization potency. **e**, Negative stain EM imaging of native-like soluble prefusion S trimer (left) or S incubated with S2H97 (right). Micrographs representative of 51 (SARS-CoV-2 S) and 173 (+S2H97) micrographs. **f**, S2H97 prophylactic efficacy in Syrian hamsters. Infectious virus titers (left) and RNA levels (right) measured in hamsters four days after SARS-CoV-2 challenge in animals prophylactically dosed with 25 mg/kg S2H97 or isotype control. Two animals with undetectable S2H97 levels (<50 ng/mL) at the time of viral challenge are marked by ‡. ** p=0.0048 (virus titer) and p=0.0048 (RNA) vs control, two-sided Mann-Whitney test (animals with no detectable serum antibody excluded). **g**, Blockade of binding[15] by sera from SARS-CoV-2-infected (top) or vaccinated (bottom) donors. Percentage of samples with blockade above the lower detection limit are indicated.
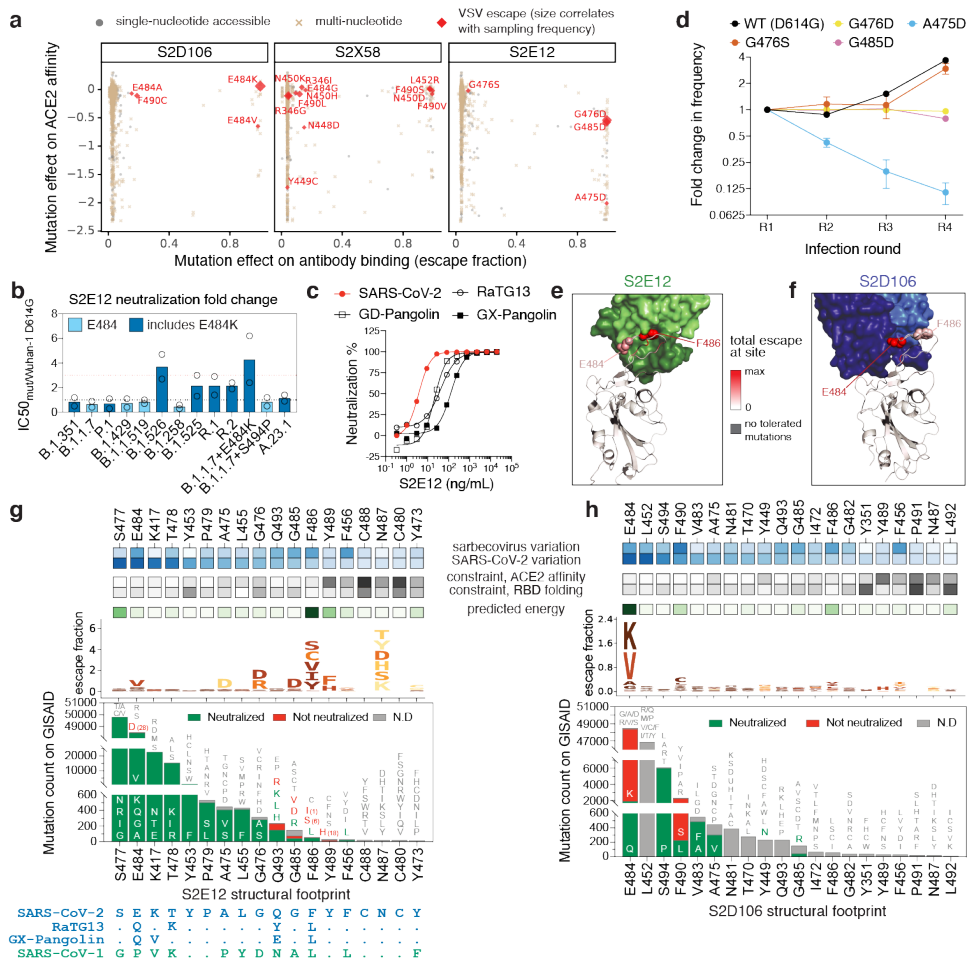
Fig. 3. Breadth and escapability among RBM antibodies. a, Escape mutations in spike-expressing VSV passaged in the presence of monoclonal antibody. Plot shows mutation effects on antibody (x-axis) and ACE2 (y-axis) binding. **b**, Neutralization of SARS-CoV-2 variants by S2E12 (spike-pseudotyped VSV on Vero E6 cells), as in Fig. 2d. **c**, S2E12 breadth of neutralization (spike-pseudotyped VSV on 293T-ACE2 cells). Points represent mean of biological duplicates. **d**, Replicative fitness of S2E12 escape mutations identified in (**a**) on Vero E6 cells. Points represent mean and error bars standard error from triplicate experiments. **e,f**, Structures of S2E12 Fab (**e**) and S2D106 Fab (**f**) bound to SARS-CoV-2 RBD. RBD sites colored by escape (scale bar, center). The E484 side chain is included for visualization purposes only but was not included in the final S2D106-bound structure due to weak density. **g,h**, Integrative features of the structural footprints (5 Å cutoff) of S2E12 (**g**) and S2D106 (**h**). Sites are ordered by the frequency of observed mutants among SARS-CoV-2 sequences on GISAID. Heatmaps as in Fig. 2b. Logoplots as in Fig. 1c, but only showing amino acid mutations accessible via single-nucleotide mutation from Wuhan-Hu-1 for comparison with (**a**). Barplots illustrate frequency of SARS-CoV-2 mutants and their validated effects on antibody neutralization (spike-pseudotyped VSV on Vero E6 cells). Red, >10-fold increase in IC50 due to mutation.
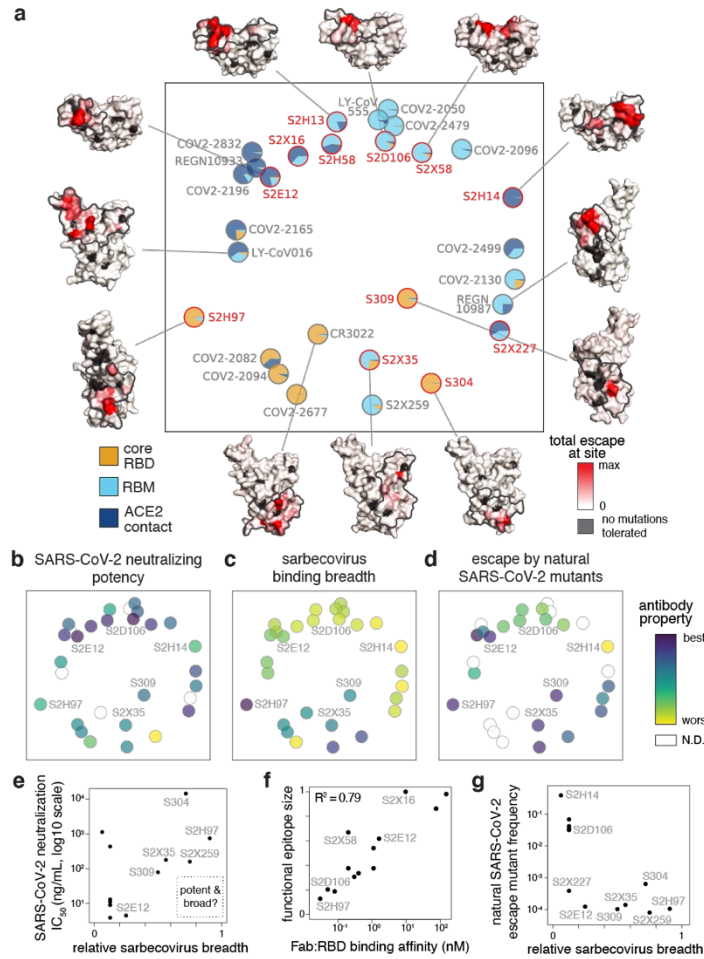
Fig. 4. Antibody epitope, potency, breadth, and escapability. a, Multidimensional scaling projection of similarities in antibody binding-escape maps from this (red) and prior (gray) studies. Pie charts illustrate the RBD sub-domains where mutations confer escape (bottom left). Structural projections of escape arrayed around the perimeter (scale bar, bottom right), with gray outlines tracing structural footprints. **b-d**, Projected epitope space from (**a**) annotated by antibody properties. For each property, antibodies are colored such that purple reflects the most desirable antibody (scale bar, right): most potent neutralization (log10 scale), highest breadth, and lowest natural frequency of escape mutants (log10 scale). **e**, Relationship between SARS-CoV-2 neutralization potency and sarbecovirus breadth for antibodies in this study and S2X259[37]. **f**, Relationship between functional epitope size and SARS-CoV-2 RBD binding affinity. **g**, Relationship between natural SARS-CoV-2 escape mutant frequency (Extended Data Fig. 3c) and sarbecovirus breadth.

a, **b**, **c**, **d**

		NTD	RBD	S1/S2	S2
B.1.351	South Africa	L18F/D80A/D215G/R246I/242-244 del	K417N/E484K/N501Y	D614G	A701V
B.1.1.7	UK	H69-/ V70-/ Y144-	N501Y	A570D/D614G/P681H	T716I/S982A/D1118H
P.1	Brazil	L18F/T20N/P26S/D138Y/R190S	K417T/E484K/N501Y	D614G/H655Y	T1027I/V1167F
B.1.429	California	S13I/W152C	L452R	D614G	
B.1.519	Mexico-Swiss		T478K	D614G/P681H	T732A
B.1.526	New York	L5F/T95I/D253G	E484K	D614G	A701V
B.1.258	UK (Scotland)	H69-/ V70-	N439K	D614G	
B.1.525	Nigeria	Q52R/A67V/H69-/V70-/Y144-	E484K	D614G/Q677H	F888L
R.1		W152L	E484K	D614G	G769V
R.2			E484K	D614G/Q677H	T732S/E1202Q
B.1.1.7+E484K	UK (Bristol)	H69-/ V70-/ Y144-	E484K/N501Y	A570D/D614G/P681H	T716I/S982A/D1118H
B.1.1.7 + S494P	UK	H69-/ V70-/ Y144-	N501Y/S494P	A570D/D614G/P681H	T716I/S982A/D1118H
A.23.1	UK (Liverpool)	R102I/F157L	V367F/E484K	Q613H/P681R	

Extended Data Fig. 1. Antibody neutralization and binding data. a, Neutralization of authentic SARS-CoV-2 (SARS-CoV-2-Nluc) by 14 antibodies. Shown are representative live virus neutralization plots, measured with entry into Vero E6 cells. Symbols are means ± SD of technical triplicates. Dashed lines indicate IC_{50} and IC_{90} values. All antibodies were measured at each concentration point in the series, with hidden points due to overplotting reflecting overlap at the upper and lower neutralization limits. **b**, Correlation in antibody neutralization IC_{50} as determined in spike-pseudotyped VSV particles (n = 3 to 8) versus authentic SARS-CoV-2 (n = 3). **c**, Representative SPR sensorgrams of Fab fragments of the six newly described antibodies binding to the SARS-CoV-2 RBD. White and gray stripes indicate association and dissociation phases, respectively. Binding affinities for previously described antibodies shown in Fig. 1a are consistent with measurements from Piccoli et al. (S304, S309, S2X35, S2H13, S2H14)[15] and Tortorici et al. (S2E12)[8]. **d**, Identifiers and spike genotypes of SARS-CoV-2 variants tested in neutralization assays in Figs. 2d and 3b.
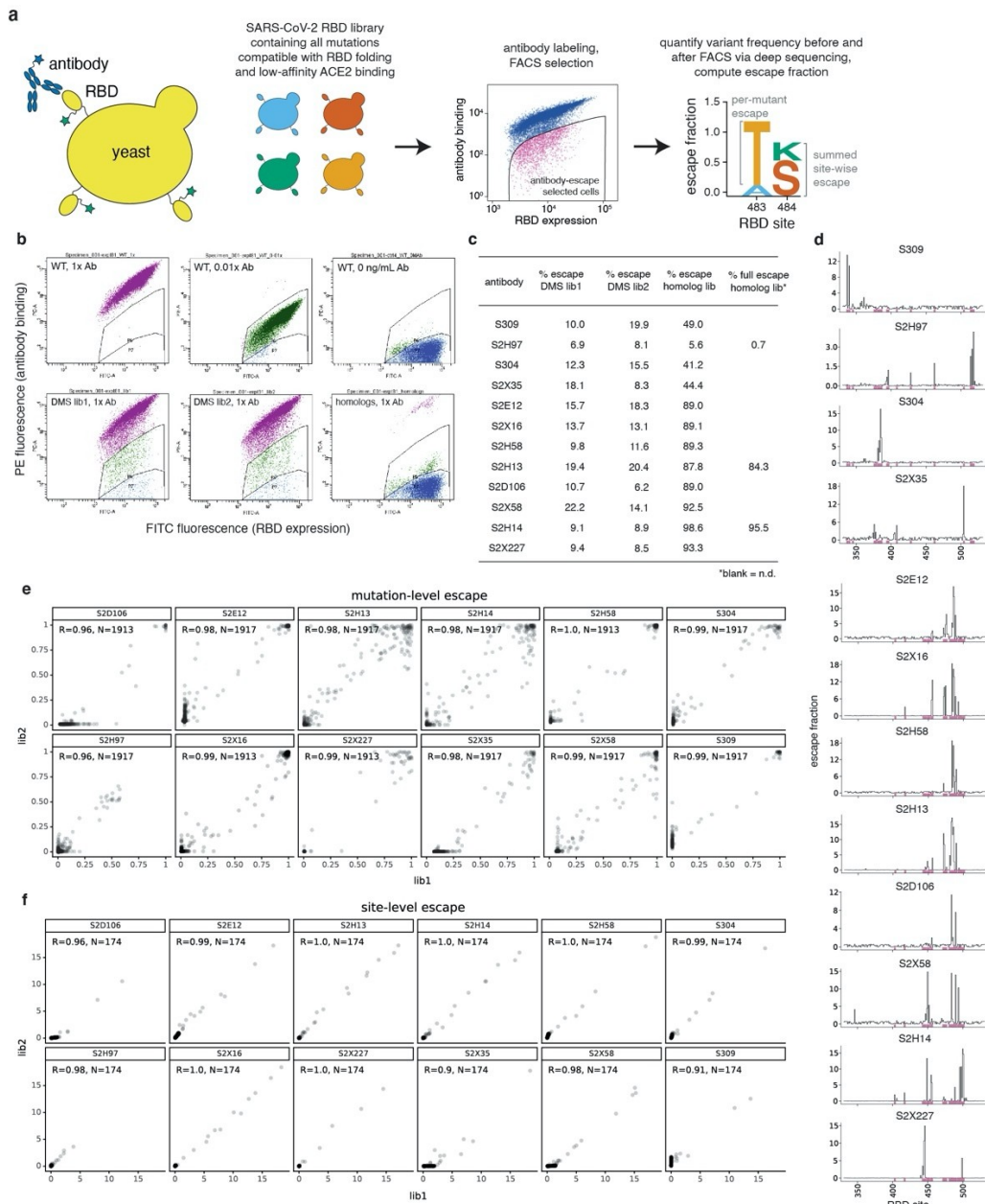
Extended Data Fig. 2. Deep mutational scanning to map mutations that escape antibody binding. a, Scheme of the deep mutational scanning assay. Conformationally intact RBD is expressed on the surface of yeast, where RBD expression and antibody binding is detectable via fluorescent labeling. We previously constructed mutant libraries containing virtually all of the 3,819 possible amino acid mutations in the SARS-CoV-2 RBD[26] and sorted the library to eliminate mutations that destabilize the RBD or strongly reduce ACE2-binding affinity[3]. We incubate the library with a sub-saturating antibody concentration and use fluorescence-activated cell sorting (FACS) to isolate yeast cells expressing RBD mutants with reduced antibody binding. Deep sequencing quantifies mutant frequencies before and after FACS selection, enabling calculation of the "escape fraction" of each amino acid mutation, which reflects the fraction of cells carrying that mutation that fall into the antibody-escape bin. Mutation escape fractions are represented in logoplots, where the height of a letter reflects the extent of escape from antibody binding. **b**, Representative selection gates, after gating for single cells expressing RBD as in Greaney et al.[3]. Yeast expressing the SARS-CoV-2 RBD (top panels) are labeled at 1x, 0.01x and no antibody to guide selection gates. Mutant RBDs that reduce binding (green, gate drawn to capture 0.01x WT control) are sorted and sequenced for calculation of mutant escape fractions. This same gate was used to quantify escape within libraries of yeast expressing all sarbecovirus RBD homologs. For several antibodies, we also selected the sarbecovirus RBD library with a more stringent "full escape" gate (blue, gate drawn to capture 0 ng/mL WT control). **c**, Fraction of library cells falling into escape bins for each antibody selection. **d**, Line plots showing total escape at all RBD sites for each antibody. Sites of strong escape illustrated in logoplots in Fig. 1b,c shown with pink indicators. **e,f**, Correlation in per-mutation (**e**) and per-site (**f**, sum of per-mutation) escape

fractions for duplicate libraries that were independently generated and assayed. *N*, number of mutations (**e**) or sites (**f**) in the correlation.
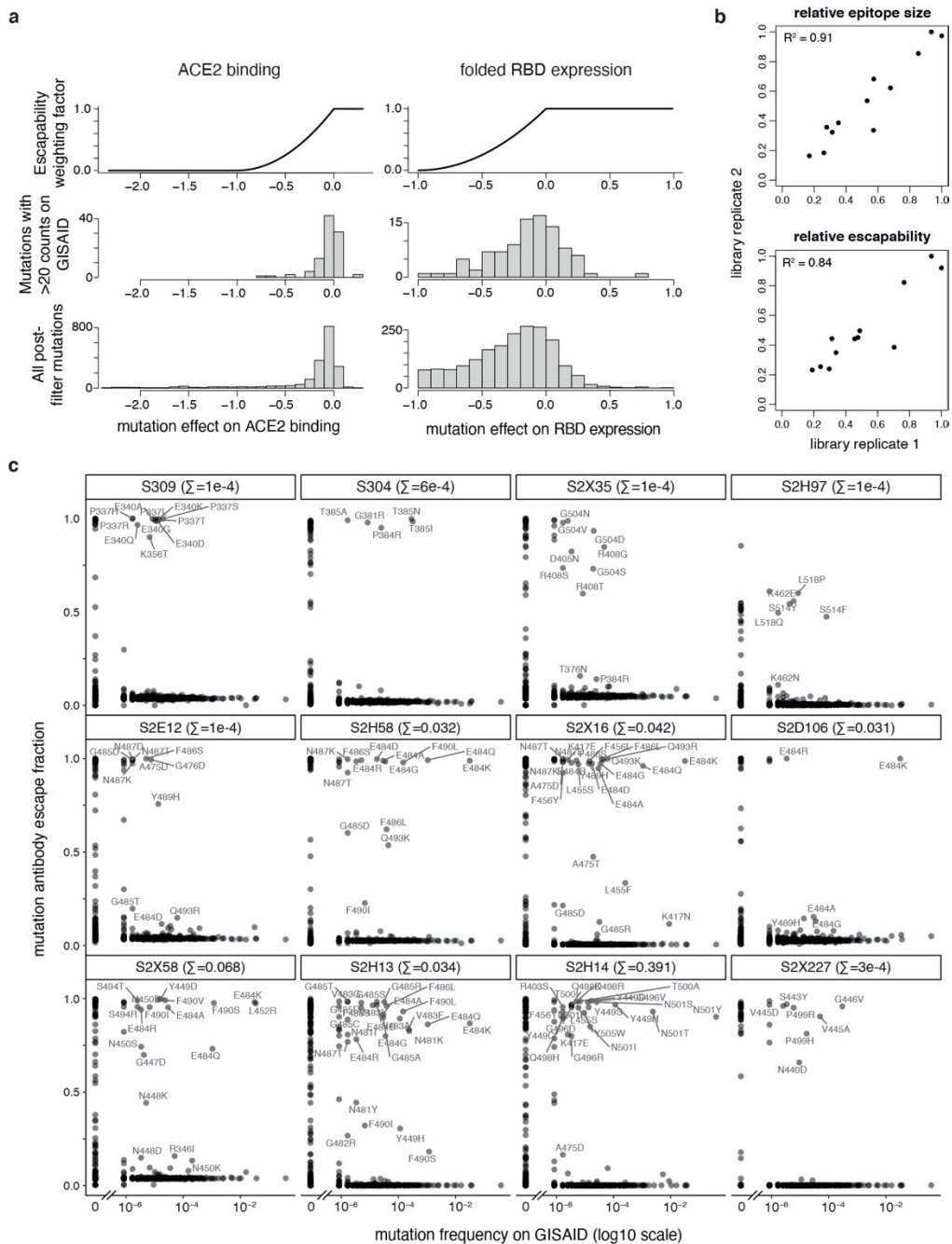
Extended Data Fig. 3. Antibody escapability from deep mutational scanning measurements and in natural SARS-CoV-2 mutants. a, To calculate antibody escapability (Fig. 1b,c), mutation escape fractions were weighted by their deleterious consequences for ACE2 binding or RBD expression. Top plots show the weighting factor (y-axis) for mutation effects on ACE2 binding (left) and RBD expression (right). This weight factor was multiplied by the mutation escape fraction in the summation to calculate antibody escapability as described in the Methods. Histograms show the distribution of mutation effects on ACE2 binding (left) and RBD expression (right) for all mutations that pass our computational filtering steps (bottom), and mutations that are found with at least 20 sequence counts on GISAID (middle). **b**, Correlation in antibody relative epitope size (top) and escapability (bottom) calculated from independent deep mutational scanning replicates, compared to the averaged replicates shown in Fig. 1b,c. R^2, squared Pearson correlation coefficient. **c**, Scatterplots illustrate the degree to which a mutation escapes antibody binding (escape fraction, y-axis) and its frequency among 1,190,241 high-quality human-derived SARS-CoV-2 sequences present on GISAID as of May 2, 2021. Large escape mutations (>5x global median escape fraction) for each antibody with non-zero mutant frequencies are labeled. Plot labels report the sum of mutant frequencies for all labeled mutations, corresponding to the natural SARS-CoV-2 mutant escape frequency for antibodies shown in Fig. 4d,g.

1136
1137 **Extended Data Fig. 4. Breadth of antibody binding across sarbecoviruses. a**, Phylogenetic relationship of sarbecovirus
1138 RBDs inferred from aligned nucleotide sequences, with the four sarbecovirus clades labeled in separate colors used
1139 throughout the text. Node support values are bootstrap support values. **b**, Breadth of sarbecovirus binding by each antibody to
1140 a panel of yeast-displayed sarbecovirus RBDs. Data as in Fig. 1d, with the addition of secondary "full escape" selection data
1141 for S2H97, S2H13, and S2H14 (0 ng/mL WT control, Extended Data Fig. 2b,c), enabling differentiation of RBDs with
1142 intermediate binding (e.g., S2H97/RsSHC014) versus complete loss of binding. Escape fractions are calculated as the mean

1143 of replicate barcoded genotypes internal to the library. Median number of barcodes per RBD is 249, with a range of 104 to
1144 566. The median SEM across escape fraction measurements is 0.019, with a range of 0.00005 to 0.038 across all
1145 RBD/antibody pairs. **c**, Flow cytometry detection of antibody binding to isogenic yeast-displayed RBD variants. **d**, Flow
1146 cytometry detection of antibody binding to mammalian-surface displayed spikes. **e**, ELISA binding of antibody to purified
1147 RBD proteins. **f**, SPR measurement of binding of cross-reactive antibodies (Fab) and human ACE2 to select sarbecovirus
1148 RBDs. NB, no binding; NT, not tested. Values from single replicates. **g**, S2H97 neutralization of VSV pseudotyped with
1149 select sarbecovirus spikes, with entry measured in ACE2-transduced BHK-21 cells. Curves are representative of two
1150 independent experiments. Points represent means, error bars standard deviation from three technical replicates, and IC50
1151 geometric mean of experiments. IC50 values are not comparable to other experiments on Vero E6 cells (e.g. Fig. 2c) due to
1152 ACE2 overexpression and its impact on S2H97 neutralization. **h**, Alignment of germline-reverted and mature S2H97 heavy-
1153 (top) and light-chain (bottom) amino acid sequences. CDR sequences shown in grey box. Heatmap overlay indicates the
1154 predicted energetic contribution of antibody paratope residues from the crystal structure. **i**, Binding of germline-reverted and
1155 mature S2H97 to select sarbecovirus RBDs as measured by SPR. **j**, Neutralization of select sarbecoviruses by S2E12 (spike-
1156 pseudotyped VSV on 293T-ACE2 cells). Details as in Fig. 3c. **k**, Alignment of germline-reverted and mature S2E12. Details
1157 as in (**h**). **l**, Binding of germline-reverted and mature S2E12 to select sarbecovirus RBDs as measured by SPR.

1158
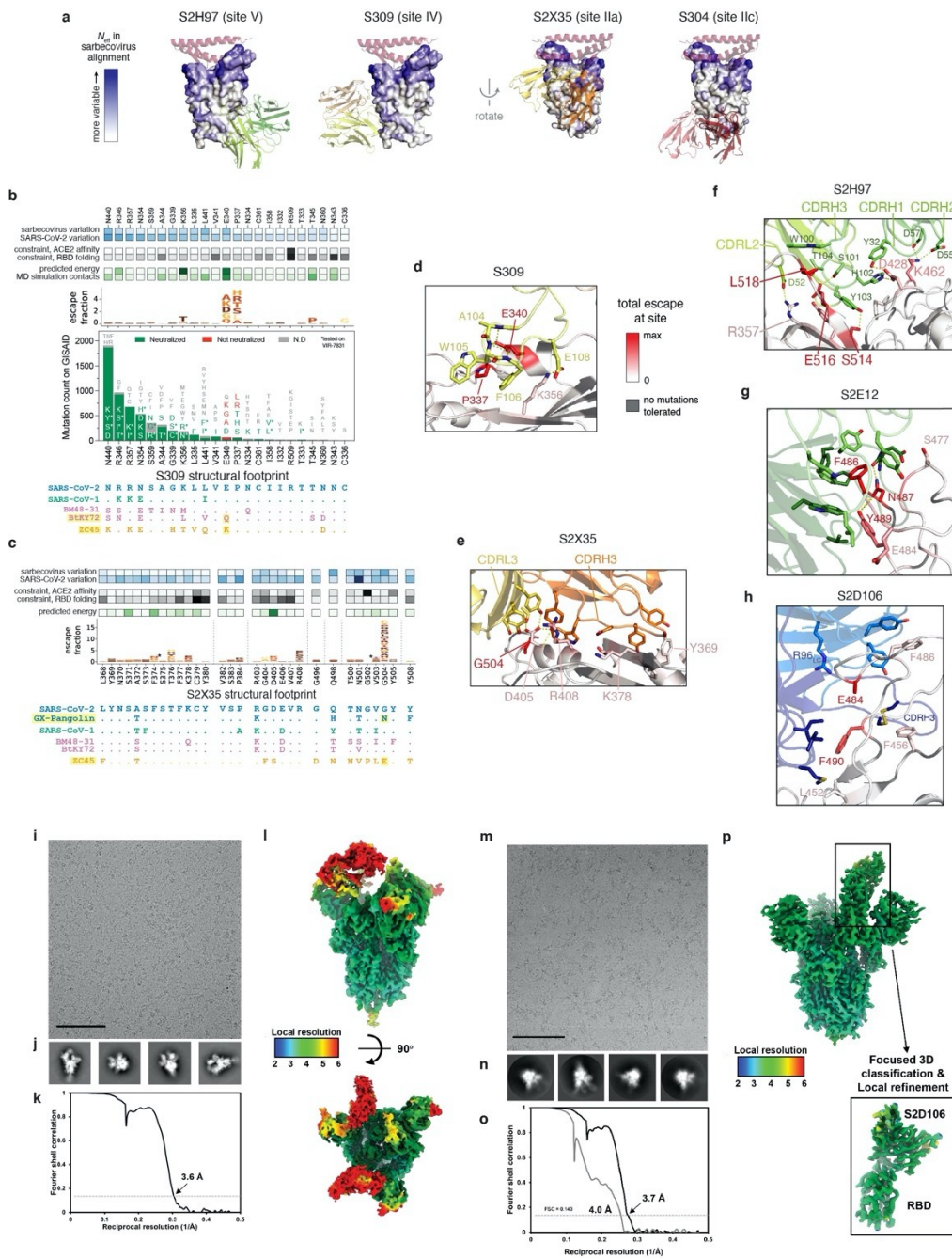
1159
1160 **Extended Data Fig. 5. Structures and epitopes of Fab:RBD complexes. a,** Surfaces targeted by broadly binding RBD
1161 antibodies. RBD surface is colored by site variability across sarbecoviruses. ACE2 key motifs shown in transparent red
1162 cartoon. Antibody variable domains shown as cartoon, with darker shade indicating the heavy chain. **b,c,** Integrative features
1163 of the S309 (**b**) and S2X35 (**c**) structural epitopes. Details as in Fig. 3g,h and Fig. 2b. **d-h,** Zoomed in view of the RBD
1164 bound to S309 (**d**), S2X35 (**e**), S2H97 (**f**), S2E12 (**g**), and S2D106 (**h**), with important contact and escape residues labeled.
1165 RBD residues colored by total site escape [scale bar, right of (**d**)]. **i,j,** Representative electron micrograph and 2D class
1166 averages of SARS-CoV-2 S in complex with the S2H97 Fab embedded in vitreous ice. Scale bar: 400 Å. Micrographs
1167 representative of 3138 micrographs. **k,** Gold-standard Fourier shell correlation curve for the S2H97-bound SARS-CoV-2 S
1168 trimer reconstruction. The 0.143 cutoff is indicated by a horizontal dashed line. **l,** Local resolution map calculated using
1169 cryoSPARC for the whole reconstruction with two orthogonal orientations. **m,n,** Representative electron micrograph and 2D
1170 class averages of SARS-CoV-2 S in complex with the S2D106 Fab embedded in vitreous ice. Scale bar: 400 Å. Micrographs
1171 representative of 2166 micrographs **o,** Gold-standard Fourier shell correlation curves for the S2D106-bound SARS-CoV-2 S
1172 trimer (black line) and locally refined RBD/S2D106 variable domains (gray line). The 0.143 cutoff is indicated by a
1173 horizontal dashed line. **p,** Local resolution map calculated using cryoSPARC for the whole reconstruction and the locally
1174 refined RBD/S2D106 variable domain region.
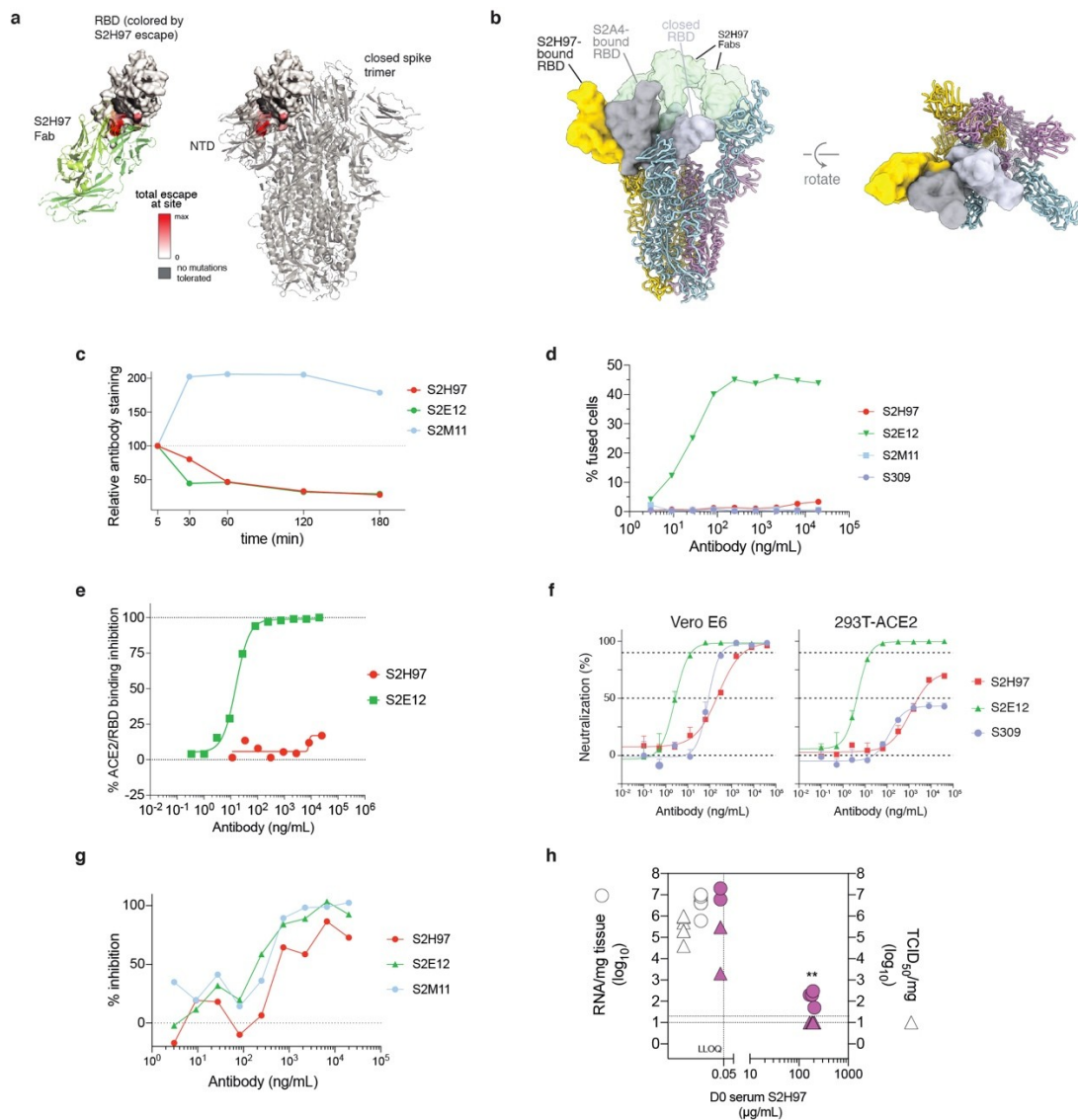
1175
Extended Data Fig. 6. Mechanism of action of S2H97 neutralization and protection. a, Quaternary context of the S2H97 epitope. Left, S2H97-bound RBD, with RBD sites colored by S2H97 escape (scale bar, bottom). Right, RBD in the same angle as left, in the closed spike trimer. **b**, CryoEM structure of S2H97 Fabs (green surfaces) bound to SARS-CoV-2 S indicating the extensive opening of the RBD (yellow surface) necessary to access the S2H97 epitope. Closed RBD (light purple surface, PDB 7K43) and site II Fab S2A4 bound open RBD (gray surface, PDB 7JVC) are shown for comparison. Spike protomers are shown in yellow, blue, and pink. **c**, Antibody-mediated S_1 shedding from cell-surface expressed SARS-CoV-2 S as determined by flow cytometry. **d**, Cell-cell fusion of CHO cells expressing SARS-CoV-2 S (CHO-S) incubated with variable concentrations of antibody. **e**, Antibody competition with RBD-ACE2 binding determined by ELISA. Points represent mean of technical duplicates. **f**, S2H97 neutralization of SARS-CoV-2 S pseudotyped VSV on ACE2-overexpressing cells (293T-ACE2) compared to Vero E6 cells. Points reflect mean and error bars reflect standard deviation from triplicate measurements. Curves are representative of two biological replicates. **g**, Antibody inhibition of cell-to-cell fusion of Vero E6 cells transfected with SARS-CoV-2 S. **h**, Influence of circulating S2H97 level on prophylactic efficacy in Syrian hamsters. Infectious virus titers (right y-axis, triangles) and RNA levels (left y-axis, circles) reflect the data represented in Fig. 2f, measured in hamsters four days after SARS-CoV-2 challenge in animals prophylactically dosed with 25 mg/kg S2H97 (magenta symbols) or isotype control (white symbols). The levels of circulating S2H97 (D0, before infection, µg/mL) are shown on the x-axis (LLOQ, lower level of quantification). ** p=0.0048 (virus titer) and p=0.0048 (RNA) vs control isotype, two-sided Mann-Whitney test (the 2 animals shown with no detectable serum antibody were excluded from the comparison).
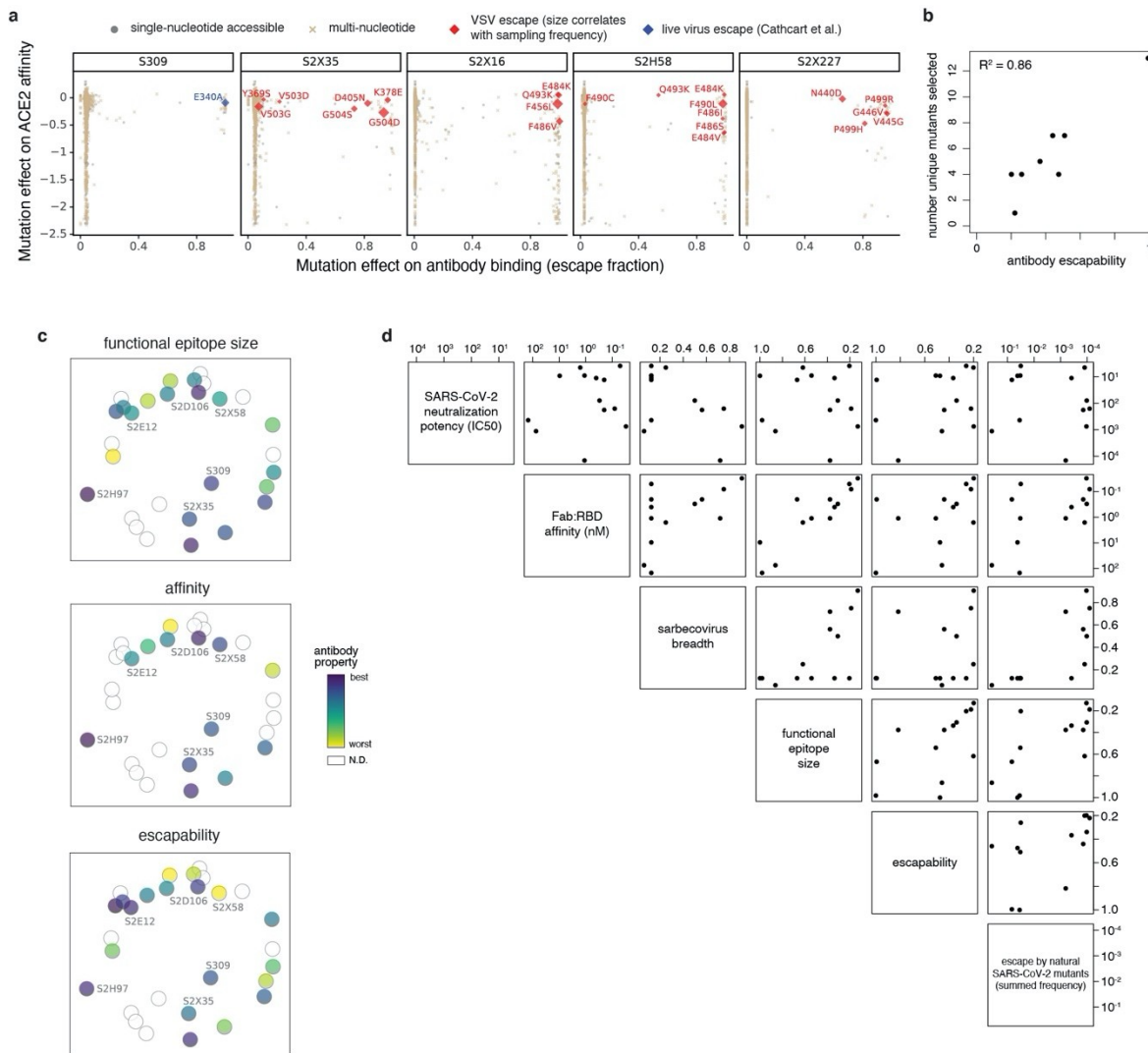
Extended Data Fig. 7 Escapability and the relationships among antibody properties. a, Additional spike-VSV viral escape selections, as in **Fig. 3a**, and an illustration of the authentic SARS-CoV-2 escape data for S309 reported in Cathcart et al.[22]. **b**, Correlation between the number of unique mutations selected across viral escape selection experiments and antibody escapability as tabulated in Fig. 1b,c, plus S2X259[37]. **c**, Projected epitope space from Fig. 4a annotated by antibody properties as in Fig. 4b-d. For each property, antibodies are colored such that purple reflects the most desirable antibody (scale bar, right; N.D., not determined): narrowest functional epitope, tightest binding affinity (K_D, log10 scale), lowest escapability. **d**, Pairwise scatterplots between all antibody properties discussed in the main text. Select scatterplots from this panel are shown in Figs. 4e-g. Details of each property described in Methods. All axes are oriented such that moving up on the y-axis and right on the x-axis corresponds to moving in the "preferred" direction for an antibody property (lower neutralization IC50, lower K_D, higher breadth, narrower epitope size, lower escapability, lower total frequency of SARS-CoV-2 escape mutants among sequences on GISAID).

Extended Data Table 1. Characteristics of the antibodies described in this study.

Mab ID	Site	Cross-reactive	ACE2 blocker	VH	HCDR3 length (amino acids)	VH identity to GL	VK/VL	IC50 (ng/mL) VSV-pp	IC90 (ng/mL)	IC50 (ng/mL) IF/luc	IC90 (ng/mL)	Spike Apparent Affinity[§] by SPR (nM) Fab	RBD Affinity by SPR (nM) (RBD ligand-Fab analyte; IgG ligand-RBD analyte) Fab	IgG	S1 shedding	Effector function	RBD open vs closed	Days from symptoms onset	Somatic Hyper Mut. HC/LC
S2E12	Ia	No	Yes	VH1-58	16	97.2%	VK3-20	2.0 (0.9-3.4)	12.4	4.5 (3-6)	14.0	2.5[†]	1.7 (1.61-1.76)	0.7	Yes	No	open	51	6/4
S2X58	Ib	No	Yes	VH1-46	12	99.0%	VK1-33	4.3 (2.7-8.8)	69.0	13.1 (7-20)	49.1	0.6	0.2 (0.20-0.24)	0.2	Yes	No	open	48	3/3
S2H58	Ib	No	Yes	VH1-2	15	97.9%	VK2-28	6.1 (1.7-15.7)	123.0	9.0 (6-11)	28.7	4.8	1.0 (0.99-1.08)	1.5	No	Yes	NA	45	6/3
S2D106	Ia	No	Yes	VH1-69	19	97.2%	VK1-39	4.3 (3.5-6.5)	25.6	6.8 (5-9)	23.6	0.17	0.05 (0.046-0.049)	0.04	Yes	No	open	98	5/3
S2X227	Ib	No	Yes	VH1-46	14	97.9%	VK4-1	5.3 (4.4-6.2)	26.9	11.2 (9-13)	36.0	0.11	0.4 (0.41-0.46)	0.1	No	Yes	NA	75	3/2
S2X16	Ia	No	Yes	VH1-69	18	97.6%	VK2-28	8.1 (2.6-14.9)	62.1	9.2 (4-16)	39.7	11.1	9.2 (8.83-9.59)	6.1[‖]	Yes	No	NA	48	3/2
S304	IIc	Yes	No	VH3-13	14	98.6%	VK1-39	9405 (8827-9795)	n/a	14412 (7573-29889)	n/a	8.7*	1.0 (0.93-1.17)	0.4	Yes	No	open	10y	5/6
S309	IV	Yes	No	VH1-18	20	97.2%	VK3-20	31.1 (23.0-58.7)	160.9	78.9 (52-121)	300.3	~0.2*	0.2 (0.17-0.31)	0.2[‡]	No	Yes	open/closed	10y	8/6
S2X35	IIa	Yes	Yes	VH1-18	21	98.6%	VL1-40	96.2 (67.8-144.9)	530.5	179.4 (121-219)	592.5	~0.1*	0.2 (0.18-0.22)	0.06	Yes	No	open	48	4/1
S2H97	V	Yes	No	VH5-51	13	98.3%	VL2-14	337.6 (277-406)	3656.1	748.7 (540-1120)	3290.7	~2	0.04 (0.031-0.060)	0.04	Yes	No	open	81	7/6
S2H13	Ib	No	Yes	VH3-7	13	97.9%	VL7-46	637.6 (494-856)	6745.9	435.3 (331-656)	1390.1	119*	123 (108-149)	33[‖]	No	Yes	open/closed	17	4/1
S2H14	Ia	No	Yes	VH3-15	17	100.0%	VL6-57	1274.0 (1027-1436)	8735.3	1130.3 (522-2583)	5121.8	90.1*	71 (56-77)	65[‖]	Yes	No	open	17	0/0

Extended Data Table 1: VH and VL percent identity refers to V gene segment identity compared to germline (as per the International Immunogenetics Information System (http://www.imgt.org/)). HCDR3 length was determined using IMGT. SARS-CoV-2 neutralization potency (authentic virus [*n*=3] and spike-pseudotyped VSV particles [*n* = 3 to 8] on Vero E6 cells), Fab:RBD binding affinities measured by SPR [*n* = 2 to 4]. Some binding affinities for previously described antibodies were measured in Piccoli et al. (S304, S309, S2X35, S2H13, S2H14)*, Tortorici et al. (S2E12)[†] and Cathcart et al. (S309)[‡]. Values in brackets are minimum and maximum determined values. [§]Spike binding data are "apparent affinity" or $K_{D,app}$, because RBD conformational dynamics affect the kinetics. S2H97 Fab binding to spike doesn't fit well to 1:1 binding, presumably because of changing epitope accessibility. [‖]Biphasic kinetics; Fit result is for fast phase

1194

Extended Data Table 2. Crystallographic data collection and refinement statistics.

	RBD/S2X35/S309 PDB 7R6W	RBD/S2H97/S2X259 PDB 7M7W	RBD/S2E12/S309/S304 PDB 7R6X
Data collection			
Space group	C222	P2$_1$	I4$_1$22
Cell dimensions			
a, b, c (Å)	106.27, 239.37, 129.81	86.19, 66.40, 237.66	245.87, 245.87, 237.31
α, β, γ (°)	90.00, 90.00, 90.00	90.00, 94.34, 90.00	90.00, 90.00, 90.00
Resolution (Å)	39.52-1.83 (1.86-1.83)	63.94-2.65 (2.70-2.65)	49.00-2.93 (2.99-2.93)
R_{merge}	0.085 (2.96)	0.149/2.494	0.295/7.868
$I / \sigma I$	16.2 (0.7)	10.9 (0.8)	13.3 (0.5)
Completeness (%)	99.6 (99.5)	98.6 (98.3)	100.00 (100.00)
Redundancy	6.7 (7.0)	6.9 (6.8)	28.9 (27.2)
Refinement			
Resolution (Å)	1.83	2.65	2.95
No. reflections	135,667	73,189	71,532
R_{work} / R_{free}	0.211/0.232	0.221/0.271	0.232/0.262
No. atoms			
Protein	8160	16,162	9,101
Ligand/ion	172	28	16
Water	584	95	3
B-factors			
Protein	39.56	75.86	116.53
Ligand/ion	75.00	84.00	122.00
Water	42.94	50.09	65.90
R.m.s. deviations			
Bond lengths (Å)	0.004	0.002	0.003
Bond angles (°)	1.259	0.817	0.936

Extended Data Table 3. CryoEM data collection, refinement, and validation statistics.

	SARS-CoV-2 S/S2D106 (EMD-24300)	SARS-CoV-2 S/S2D106 (local refinement) (EMD-24299) (PDB 7R7N)	SARS-CoV-2 S/S2H97 (EMD-24301)
Data collection and processing			
Magnification	130,000	130,000	36,000
Voltage (kV)	300	300	200
Electron exposure (e–/Å^2)	70	70	60
Defocus range (μm)	-0.5 – -2.5	-0.5 – -2.5	-0.5 – -3.0
Pixel size (Å)	0.525	0.525	1.16
Symmetry imposed	C1	C1	C1
Initial particle images (no.)	175,479	87,587	98,950
Map resolution (Å)	3.7	4.0	3.6
FSC threshold	0.143	0.143	0.143
Map sharpening B factor (Å^2)	-61	-17	-70
Validation			
MolProbity score		0.89	
Clashscore		0.58	
Poor rotamers (%)		0.45	
Ramachandran plot			
Favored (%)		96.78	
Allowed (%)		3.22	
Disallowed (%)		0	

REFERENCES

1. Liu, Z. *et al.* Identification of SARS-CoV-2 spike mutations that attenuate monoclonal and serum antibody neutralization. *Cell Host Microbe* **29**, 477-488.e4 (2021).
2. Weisblum, Y. *et al.* Escape from neutralizing antibodies by SARS-CoV-2 spike protein variants. *Elife* **9**, e61312 (2020).
3. Greaney, A. J. *et al.* Complete Mapping of Mutations to the SARS-CoV-2 Spike Receptor-Binding Domain that Escape Antibody Recognition. *Cell Host Microbe* **29**, 44-57.e9 (2021).
4. Pinto, D. *et al.* Cross-neutralization of SARS-CoV-2 by a human monoclonal SARS-CoV antibody. *Nature* **583**, 290–295 (2020).
5. Rappazzo, C. G. *et al.* Broad and potent activity against SARS-like viruses by an engineered human monoclonal antibody. *Science* **371**, 823–829 (2021).
6. Menachery, V. D. *et al.* A SARS-like cluster of circulating bat coronaviruses shows potential for human emergence. *Nat. Med.* **21**, 1508–1513 (2015).
7. Letko, M., Marzi, A. & Munster, V. Functional assessment of cell entry and receptor usage for SARS-CoV-2 and other lineage B betacoronaviruses. *Nat Microbiol* **5**, 562–569 (2020).
8. Tortorici, M. A. *et al.* Ultrapotent human antibodies protect against SARS-CoV-2 challenge via multiple mechanisms. *Science* **370**, 950–957 (2020).
9. Barnes, C. O. *et al.* SARS-CoV-2 neutralizing antibody structures inform therapeutic strategies. *Nature* **588**, 682–687 (2020).
10. Zost, S. J. *et al.* Potently neutralizing and protective human antibodies against SARS-CoV-2. *Nature* **584**, 443–449 (2020).
11. Hassan, A. O. *et al.* A SARS-CoV-2 Infection Model in Mice Demonstrates Protection by Neutralizing Antibodies. *Cell* **182**, 744-753.e4 (2020).
12. Winkler, E. S. *et al.* Human neutralizing antibodies against SARS-CoV-2 require intact Fc effector functions for optimal therapeutic protection. *Cell* **184**, 1804-1820.e16 (2021).
13. Schäfer, A. *et al.* Antibody potency, effector function, and combinations in protection and therapy for SARS-CoV-2 infection in vivo. *J. Exp. Med.* **218**, (2021).
14. Corti, D., Purcell, L. A., Snell, G. & Veesler, D. Tackling COVID-19 with neutralizing monoclonal antibodies. *Cell* **184**, (2021).
15. Piccoli, L. *et al.* Mapping Neutralizing and Immunodominant Sites on the SARS-CoV-2 Spike Receptor-Binding Domain by Structure-Guided High-Resolution Serology. *Cell* **183**, 1024-1042.e21 (2020).
16. Greaney, A. J. *et al.* Comprehensive mapping of mutations in the SARS-CoV-2 receptor-binding domain that affect recognition by polyclonal human plasma antibodies. *Cell Host Microbe* **29**, 463-476.e6 (2021).
17. Chen, R. E. *et al.* Resistance of SARS-CoV-2 variants to neutralization by monoclonal and serum-derived polyclonal antibodies. *Nat. Med.* **27**, 717–726 (2021).
18. Wang, P. *et al.* Antibody resistance of SARS-CoV-2 variants B.1.351 and B.1.1.7. *Nature* **593**, 130–135 (2021).
19. Thomson, E. C. *et al.* Circulating SARS-CoV-2 spike N439K variants maintain fitness while evading antibody-mediated immunity. *Cell* **184**, 1171-1187.e20 (2021).
20. Starr, T. N. *et al.* Prospective mapping of viral mutations that escape antibodies used to treat COVID-19. *Science* **371**, 850–854 (2021).
21. Starr, T. N., Greaney, A. J., Dingens, A. S. & Bloom, J. D. Complete map of SARS-CoV-2 RBD mutations that escape the monoclonal antibody LY-CoV555 and its cocktail with LY-CoV016. *Cell Rep Med* **2**, 100255 (2021).

22. Cathcart, A. L. *et al.* The dual function monoclonal antibodies VIR-7831 and VIR-7832 demonstrate potent in vitro and in vivo activity against SARS-CoV-2. *bioRxiv* 2021.03.09.434607 (2021) doi:10.1101/2021.03.09.434607.

23. McCallum, M. *et al.* SARS-CoV-2 immune evasion by variant B.1.427/B.1.429. *bioRxiv* (2021) doi:10.1101/2021.03.31.437925.

24. Gupta, A. *et al.* Early Covid-19 treatment with SARS-CoV-2 neutralizing antibody sotrovimab. *medRxiv* (2021) doi:10.1101/2021.05.27.21257096.

25. Dingens, A. S., Arenz, D., Weight, H., Overbaugh, J. & Bloom, J. D. An Antigenic Atlas of HIV-1 Escape from Broadly Neutralizing Antibodies Distinguishes Functional and Structural Epitopes. *Immunity* **50**, 520-532.e3 (2019).

26. Starr, T. N. *et al.* Deep Mutational Scanning of SARS-CoV-2 Receptor Binding Domain Reveals Constraints on Folding and ACE2 Binding. *Cell* **182**, 1295-1310.e20 (2020).

27. Faria, N. R. *et al.* Genomics and epidemiology of a novel SARS-CoV-2 lineage in Manaus, Brazil. *medRxiv* 2021.02.26.21252554 (2021).

28. Tegally, H. *et al.* Detection of a SARS-CoV-2 variant of concern in South Africa. *Nature* **592**, 438–443 (2021).

29. Zhang, W. *et al.* Emergence of a Novel SARS-CoV-2 Variant in Southern California. *JAMA* (2021) doi:10.1001/jama.2021.1612.

30. Walls, A. C. *et al.* Unexpected Receptor Functional Mimicry Elucidates Activation of Coronavirus Fusion. *Cell* **176**, 1026-1039.e15 (2019).

31. Lempp, F. A. *et al.* Membrane lectins enhance SARS-CoV-2 infection and influence the neutralizing activity of different classes of antibodies. *bioRxiv* 2021.04.03.438258 (2021) doi:10.1101/2021.04.03.438258.

32. Pinto, D. *et al.* A human antibody that broadly neutralizes betacoronaviruses protects against SARS-CoV-2 by blocking the fusion machinery. *bioRxiv* 2021.05.09.442808 (2021) doi:10.1101/2021.05.09.442808.

33. Walls, A. C. *et al.* Elicitation of Potent Neutralizing Antibody Responses by Designed Protein Nanoparticle Vaccines for SARS-CoV-2. *Cell* **183**, 1367-1382.e17 (2020).

34. Cohen, A. A. *et al.* Mosaic nanoparticles elicit cross-reactive immune responses to zoonotic coronaviruses in mice. *Science* **371**, 735–741 (2021).

35. Saunders, K. O. *et al.* Neutralizing antibody vaccine for pandemic and pre-emergent coronaviruses. *Nature* (2021) doi:10.1038/s41586-021-03594-0.

36. Dong, J. *et al.* Genetic and structural basis for recognition of SARS-CoV-2 spike protein by a two-antibody cocktail. *bioRxiv* 2021.01.27.428529 (2021) doi:10.1101/2021.01.27.428529.

37. Tortorici, M. A. *et al.* Structural basis for broad sarbecovirus neutralization by a human monoclonal antibody. *bioRxiv* 2021.04.07.438818 (2021) doi:10.1101/2021.04.07.438818.

38. Sauer, M. M. *et al.* Structural basis for broad coronavirus neutralization. *Nat. Struct. Mol. Biol.* (2021) doi:10.1038/s41594-021-00596-4.

39. Kistler, K. E. & Bedford, T. Evidence for adaptive evolution in the receptor-binding domain of seasonal coronaviruses OC43 and 229e. *Elife* **10**, (2021).

40. Eguia, R. T. *et al.* A human coronavirus evolves antigenically to escape antibody immunity. *PLoS Pathog.* **17**, e1009453 (2021).

41. Walls, A. C. *et al.* Elicitation of broadly protective sarbecovirus immunity by receptor-binding domain nanoparticle vaccines. *bioRxiv* 2021.03.15.435528 (2021) doi:10.1101/2021.03.15.435528.

42. Zhou, P. *et al.* A protective broadly cross-reactive human antibody defines a conserved site of vulnerability on beta-coronavirus spikes. *bioRxiv* 2021.03.30.437769 (2021) doi:10.1101/2021.03.30.437769.

43. Crawford, K. H. D. *et al.* Protocol and Reagents for Pseudotyping Lentiviral Particles with SARS-CoV-2 Spike Protein for Neutralization Assays. *Viruses* **12**, (2020).

44. Xie, X. *et al.* A nanoluciferase SARS-CoV-2 for rapid neutralization testing and screening of anti-infective drugs for COVID-19. *Nat. Commun.* **11**, 5214 (2020).

45. Takada, A. *et al.* A system for functional analysis of Ebola virus glycoprotein. *Proc. Natl. Acad. Sci. U. S. A.* **94**, 14764–14769 (1997).

46. Riblett, A. M. *et al.* A Haploid Genetic Screen Identifies Heparan Sulfate Proteoglycans Supporting Rift Valley Fever Virus Infection. *J. Virol.* **90**, 1414–1423 (2016).

47. Giroglou, T. *et al.* Retroviral vectors pseudotyped with severe acute respiratory syndrome coronavirus S protein. *J. Virol.* **78**, 9007–9015 (2004).

48. Collier, D. A. *et al.* Sensitivity of SARS-CoV-2 B.1.1.7 to mRNA vaccine-elicited antibodies. *Nature* **593**, 136–141 (2021).

49. Walls, A. C. *et al.* Structure, Function, and Antigenicity of the SARS-CoV-2 Spike Glycoprotein. *Cell* **181**, 281-292.e6 (2020).

50. Otwinowski, J., McCandlish, D. M. & Plotkin, J. B. Inferring the shape of global epistasis. *Proc. Natl. Acad. Sci. U. S. A.* **115**, E7550–E7558 (2018).

51. Hilton, S. *et al.* dms-view: Interactive visualization tool for deep mutational scanning data. *J. Open Source Softw.* **5**, 2353 (2020).

52. Song, H.-D. *et al.* Cross-host evolution of severe acute respiratory syndrome coronavirus in palm civet and human. *Proc. Natl. Acad. Sci. U. S. A.* **102**, 2430–2435 (2005).

53. Tong, S. *et al.* Detection of novel SARS-like and other coronaviruses in bats from Kenya. *Emerg. Infect. Dis.* **15**, 482–485 (2009).

54. Zhou, H. *et al.* A Novel Bat Coronavirus Closely Related to SARS-CoV-2 Contains Natural Insertions at the S1/S2 Cleavage Site of the Spike Protein. *Curr. Biol.* **30**, 2196-2203.e3 (2020).

55. Lam, T. T.-Y. *et al.* Identifying SARS-CoV-2-related coronaviruses in Malayan pangolins. *Nature* **583**, 282–285 (2020).

56. Katoh, K. & Standley, D. M. MAFFT multiple sequence alignment software version 7: improvements in performance and usability. *Mol. Biol. Evol.* **30**, 772–780 (2013).

57. Suyama, M., Torrents, D. & Bork, P. PAL2NAL: robust conversion of protein sequence alignments into the corresponding codon alignments. *Nucleic Acids Res.* **34**, W609-12 (2006).

58. Stamatakis, A. RAxML version 8: a tool for phylogenetic analysis and post-analysis of large phylogenies. *Bioinformatics* **30**, 1312–1313 (2014).

59. Elbe, S. & Buckland-Merrett, G. Data, disease and diplomacy: GISAID's innovative contribution to global health. *Glob Chall* **1**, 33–46 (2017).

60. Lan, J. *et al.* Structure of the SARS-CoV-2 spike receptor-binding domain bound to the ACE2 receptor. *Nature* **581**, 215–220 (2020).

61. Yuan, M. *et al.* A highly conserved cryptic epitope in the receptor binding domains of SARS-CoV-2 and SARS-CoV. *Science* **368**, 630–633 (2020).

62. Hansen, J. *et al.* Studies in humanized mice and convalescent humans yield a SARS-CoV-2 antibody cocktail. *Science* **369**, 1010–1014 (2020).

63. Shi, R. *et al.* A human neutralizing antibody targets the receptor-binding site of SARS-CoV-2. *Nature* **584**, 120–124 (2020).

64. Kabsch, W. XDS. *Acta Crystallogr. D Biol. Crystallogr.* **66**, 125–132 (2010).

65. McCoy, A. J. *et al.* Phaser crystallographic software. *J. Appl. Crystallogr.* **40**, 658–674 (2007).

66. Emsley, P., Lohkamp, B., Scott, W. G. & Cowtan, K. Features and development of coot. *Acta Crystallogr. D Biol. Crystallogr.* **66**, 486–501 (2010).

67. Croll, T. I. ISOLDE: a physically realistic environment for model building into low-resolution electron-density maps. *Acta Crystallogr. D Struct. Biol.* **74**, 519–530 (2018).

68. Murshudov, G. N. *et al.* REFMAC5 for the refinement of macromolecular crystal structures. *Acta Crystallogr. D Biol. Crystallogr.* **67**, 355–367 (2011).

69. Hsieh, C.-L. *et al.* Structure-based design of prefusion-stabilized SARS-CoV-2 spikes. *Science* **369**, 1501–1505 (2020).

70. Suloway, C. *et al.* Automated molecular microscopy: the new Leginon system. *J. Struct. Biol.* **151**, 41–60 (2005).

71. Tegunov, D. & Cramer, P. Real-time cryo-electron microscopy data preprocessing with Warp. *Nat. Methods* **16**, 1146–1152 (2019).

72. Punjani, A., Rubinstein, J. L., Fleet, D. J. & Brubaker, M. A. cryoSPARC: algorithms for rapid unsupervised cryo-EM structure determination. *Nat. Methods* **14**, 290–296 (2017).

73. Zivanov, J. *et al.* New tools for automated high-resolution cryo-EM structure determination in RELION-3. *Elife* **7**, (2018).

74. Punjani, A., Zhang, H. & Fleet, D. J. Non-uniform refinement: adaptive regularization improves single-particle cryo-EM reconstruction. *Nat. Methods* **17**, 1214–1221 (2020).

75. Zivanov, J., Nakane, T. & Scheres, S. H. W. A Bayesian approach to beam-induced motion correction in cryo-EM single-particle analysis. *IUCrJ* **6**, 5–17 (2019).

76. Ramlaul, K., Palmer, C. M., Nakane, T. & Aylett, C. H. S. Mitigating local over-fitting during single particle reconstruction with SIDESPLITTER. *J. Struct. Biol.* **211**, 107545 (2020).

77. Pettersen, E. F. *et al.* UCSF ChimeraX: Structure visualization for researchers, educators, and developers. *Protein Sci.* **30**, 70–82 (2021).

78. Casañal, A., Lohkamp, B. & Emsley, P. Current developments in Coot for macromolecular model building of Electron Cryo-microscopy and Crystallographic Data. *Protein Sci.* **29**, 1069–1078 (2020).

79. Wang, R. Y.-R. *et al.* Automated structure refinement of macromolecular assemblies from cryo-EM maps using Rosetta. *Elife* **5**, (2016).

80. McCallum, M. *et al.* N-terminal domain antigenic mapping reveals a site of vulnerability for SARS-CoV-2. *Cell* (2021) doi:10.1016/j.cell.2021.03.028.

81. Boudewijns, R. *et al.* STAT2 signaling restricts viral dissemination but drives severe pneumonia in SARS-CoV-2 infected hamsters. *Nat. Commun.* **11**, 5838 (2020).

82. Sanchez-Felipe, L. *et al.* A single-dose live-attenuated YF17D-vectored SARS-CoV-2 vaccine candidate. *Nature* **590**, 320–325 (2021).

83. Reed, L. J. & Muench, H. A simple method of estimating fifty percent endpoints. *Am. J. Epidemiol.* **27**, 493–497 (1938).

84. Case, J. B. *et al.* Neutralizing Antibody and Soluble ACE2 Inhibition of a Replication-Competent VSV-SARS-CoV-2 and a Clinical Isolate of SARS-CoV-2. *Cell Host Microbe* **28**, 475-485.e5 (2020).

85. Shajahan, A. *et al.* Comprehensive characterization of N- and O- glycosylation of SARS-CoV-2 human receptor angiotensin converting enzyme 2. *Glycobiology* (2020) doi:10.1093/glycob/cwaa101.

86. Watanabe, Y., Allen, J. D., Wrapp, D., McLellan, J. S. & Crispin, M. Site-specific glycan analysis of the SARS-CoV-2 spike. *Science* **369**, 330–333 (2020).

87. Harbison, A. M., Brosnan, L. P., Fenlon, K. & Fadda, E. Sequence-to-structure dependence of isolated IgG Fc complex biantennary N-glycans: a molecular dynamics study. *Glycobiology* **29**, 94–103 (2019).

88. D.A. Case, K. Belfon, I.Y. Ben-Shalom, S.R. Brozell, D.S. Cerutti, T.E. Cheatham, III, V.W.D. Cruzeiro, T.A. Darden, R.E. Duke, G. Giambasu, M.K. Gilson, H. Gohlke, A.W. Goetz, R. Harris, S. Izadi, S.A. Izmailov, K. Kasavajhala, A. Kovalenko, R. Krasny, T. Kurtzman, T.S. Lee, S. LeGrand, P. Li, C. Lin, J. Liu, T. Luchko, R. Luo, V. Man, K.M. Merz, Y. Miao, O. Mikhailovskii, G. Monard, H. Nguyen, A. Onufriev, F.Pan, S. Pantano, R. Qi, D.R. Roe, A. Roitberg, C. Sagui, S. Schott-Verdugo, J. Shen, C. Simmerling, N.R.Skrynnikov, J. Smith, J. Swails, R.C. Walker, J. Wang, L. Wilson, R.M. Wolf, X. Wu, Y. Xiong, Y. Xue, D.M. York and P.A. Kollman. Amber 2020. (2020).

89. Maier, J. A. *et al.* Ff14SB: Improving the accuracy of protein side chain and backbone parameters from ff99SB. *J. Chem. Theory Comput.* **11**, 3696–3713 (2015).

90. Kirschner, K. N. *et al.* GLYCAM06: a generalizable biomolecular force field. Carbohydrates. *J. Comput. Chem.* **29**, 622–655 (2008).

91. Jorgensen, W. L., Chandrasekhar, J., Madura, J. D., Impey, R. W. & Klein, M. L. Comparison of simple potential functions for simulating liquid water. *J. Chem. Phys.* **79**, 926–935 (1983).

92. Li, P., Song, L. F. & Merz, K. M., Jr. Systematic parameterization of monovalent ions employing the nonbonded model. *J. Chem. Theory Comput.* **11**, 1645–1657 (2015).

93. Leimkuhler, B. & Matthews, C. Robust and efficient configurational molecular sampling via Langevin dynamics. *J. Chem. Phys.* **138**, 174102 (2013).

94. Darden, T., York, D. & Pedersen, L. Particle mesh Ewald: An N·log(N) method for Ewald sums in large systems. *J. Chem. Phys.* **98**, 10089–10092 (1993).

95. Shirts, M. & Pande, V. S. COMPUTING: Screen savers of the world unite! *Science* **290**, 1903–1904 (2000).

96. Zimmerman, M. I. *et al.* Citizen scientists create an Exascale computer to combat COVID-19. *bioRxivorg* (2020) doi:10.1101/2020.06.27.175430.

97. McGibbon, R. T. *et al.* MDTraj: A modern open library for the analysis of molecular dynamics trajectories. *Biophys. J.* **109**, 1528–1532 (2015).

98. Michaud-Agrawal, N., Denning, E. J., Woolf, T. B. & Beckstein, O. MDAnalysis: a toolkit for the analysis of molecular dynamics simulations. *J. Comput. Chem.* **32**, 2319–2327 (2011).

99. Gowers, R. *et al.* MDAnalysis: A python package for the rapid analysis of molecular dynamics simulations. in *Proceedings of the 15th Python in Science Conference* (SciPy, 2016). doi:10.25080/majora-629e541a-00e.